

Chiba University  
Graduate School of Science and Engineering  
**Master's Thesis**

**Detection efficiency of next  
generation IceCube optical  
module, D-Egg, and its  
sensitivity to optical  
properties of the Antarctic  
ice with the GEANT4 based  
precise photon simulation**

Submitted in March, 2020

Division of Advanced Science and Engineering  
Department of Physics

**Ayumi Kiriki**

# Abstract

IceCube is a cubic-kilometer neutrino detector located at the geographic South Pole, which consists of 5160 optical modules in the Antarctic ice sheet. These optical modules detect Cherenkov radiation induced by charged particles produced by neutrinos interacting in the Earth. Deployment of IceCube's optical modules utilises a hot water drill, where the optical modules are dropped into the water to be re-frozen in the deep ice. While the optical properties of the glacial ice have been well documented, studies of the man-made refrozen ice, called "hole ice", remain inconclusive. This has resulted in large systematic uncertainties in the angular reconstruction of neutrinos with energies between 1–10 GeV. The IceCube Upgrade array is planned for construction in the 2022/2023 South Pole Summer, involving the deployment of a new specially-designed optical module called the D-Egg. One of the important topics of the Upgrade is measurements of the optical properties of the hole ice. A GEANT4 based precise photon propagation simulation was developed and the angular dependence of the D-Egg's Cherenkov photon detection efficiency was calculated. Furthermore, a detailed hole ice simulation was performed with D-Eggs as the chosen optical modules. A maximum likelihood was constructed using various hole ice parameters, the results of which increase current understanding of the hole ice and improve on previous measurements. This simulation study shows that the D-Egg will allow IceCube to measure the optical properties of the hole ice when combined with an artificial light source, located inside the D-Egg module.

# Acknowledgments

Firstly, I would like to thank my supervisor Prof. Ishihara for her continuous support and leading me in the right direction in my research. I would like to thank to Prof. Yoshida for his accurate advises on my research. I would also like to thank Assistant Prof. Mase for his support and knowledge of the calibration of IceCube.

I would also like to thank all the members of IceCube Chiba group. Postdocs taught me a lot of things from the basics and helped me do research. Students helped me do experiments and I had a great time with them.

Finally, I want to thank my family, especially my parents for providing me an environment where I could concentrate on my research.

# Contents

<b>1</b>	<b>Introduction</b>	<b>1</b>
<b>2</b>	<b>IceCube</b>	<b>3</b>
2.1	Introduction to high-energy neutrino astronomy . . . . .	3
2.1.1	High-energy astrophysical neutrinos . . . . .	4
2.2	The IceCube experiment . . . . .	4
2.2.1	Detector . . . . .	5
2.2.1.1	IceCube array . . . . .	5
2.2.1.2	DOM—Digital Optical Module . . . . .	5
2.2.1.3	Construction . . . . .	7
2.2.2	Neutrino detection principle in IceCube . . . . .	7
2.2.2.1	Neutrino interactions . . . . .	7
2.2.2.2	Cherenkov light . . . . .	8
2.2.3	Event types . . . . .	9
2.2.3.1	Track like event . . . . .	9
2.2.3.2	Cascade event . . . . .	9
2.2.3.3	Double Bang . . . . .	9
2.2.4	Ice properties . . . . .	10
2.2.4.1	Bulk ice . . . . .	10
2.2.4.2	Hole ice . . . . .	10
2.3	IceCube Upgrade . . . . .	12
<b>3</b>	<b>D-Egg</b>	<b>14</b>
3.1	Overview . . . . .	14
3.2	PMT . . . . .	16
3.2.1	Gain . . . . .	16
3.2.2	Linearity response curve . . . . .	21
3.2.3	Detection uniformity . . . . .	21
3.2.4	Darknoise rate . . . . .	21
3.3	Glass and gel . . . . .	24

3.4	Flasher . . . . .	25
<b>4</b>	<b>Detector simulation</b>	<b>27</b>
4.1	DOMINANT . . . . .	27
4.2	DOMINANT for D-Egg . . . . .	27
4.3	Effective area calculation . . . . .	27
<b>5</b>	<b>Sensitivity to the hole ice</b>	<b>32</b>
5.1	Introduction . . . . .	32
5.2	Simulation of photon propagation in ice . . . . .	33
5.2.1	Modeling hole ice . . . . .	33
5.2.2	Modeling of Mie scattering . . . . .	33
5.2.3	Toy simulation . . . . .	34
5.2.4	Photon detection with D-Egg . . . . .	40
5.2.4.1	Simulation framework . . . . .	40
5.2.4.2	Light source . . . . .	40
5.2.4.3	Detection efficiency . . . . .	41
5.2.4.4	Results – Hole ice parameter dependence of NPE . . . . .	42
5.3	Systematic uncertainties . . . . .	46
5.3.1	Detector response . . . . .	46
5.3.2	Alignment of the D-Eggs . . . . .	46
5.3.3	Flasher LED profiles . . . . .	47
5.3.4	Cable shadow . . . . .	47
5.3.5	$\langle \cos \theta \rangle$ . . . . .	48
5.4	Extraction of hole ice parameters . . . . .	48
5.4.1	Analysis method . . . . .	48
5.4.1.1	Likelihood construction . . . . .	48
5.4.1.2	Test statistic . . . . .	50
5.4.1.3	Test data . . . . .	50
5.5	Results . . . . .	52
5.5.1	Case study – Three scenarios . . . . .	52
5.5.2	A case when the geometrical information is available . . . . .	52
5.5.3	A case when no external information is available . . . . .	53
5.5.4	Final result: all systematic uncertainties included . . . . .	53
5.5.5	Discussion . . . . .	57
5.6	Conclusion . . . . .	59
<b>6</b>	<b>Conclusion</b>	<b>60</b>
	<b>References</b>	<b>60</b>

# List of Figures

2.1	Sketch of the IceCube detector. . . . .	6
2.2	A schematic of the DOM. . . . .	6
2.3	Cherenkov light yield. . . . .	8
2.4	Depth dependence of the scattering and absorption length. . . . .	10
2.5	Hole ice forming images. . . . .	11
2.6	Camera image looking downward into the established hole ice. . . . .	12
2.7	Sketch of the planned IceCube Upgrade array. . . . .	13
3.1	Latest prototype of a complete D-Egg. . . . .	15
3.2	Latest prototype of a lower half D-Egg. . . . .	15
3.3	8" Hamamatsu R5912-100-70 PMT. . . . .	16
3.4	QE of all PMTs planned for the IceCube Upgrade measured by Hamamatsu. . . . .	17
3.5	Example of a SPE waveform. . . . .	18
3.6	Example of a PMT's charge distributions. . . . .	19
3.7	Example of a PMT's charge resolution and peak to valley ratio. . . . .	20
3.8	Example of a PMT's high voltage dependence of gain. . . . .	20
3.9	Example of a PMT's linearity response curve. . . . .	22
3.10	2D uniformity measurement setup. . . . .	23
3.11	Example of a PMT's detection uniformity. . . . .	23
3.12	Example of a PMT's darknoise rate. . . . .	24
3.13	Transmittance of the glass and gel of the D-Egg compared with the DOM. . . . .	25
3.14	Prototype of the flasher module. . . . .	26
4.1	Designs and geometries of the D-Egg implemented into DOM- INANT. . . . .	28
4.2	Wavelength dependence of the absorption length of the bulk ice. . . . .	29
4.3	Depiction of the simulation. . . . .	30

4.4	Zenith angle dependence of the effective area of the DOM and the D-Egg. . . . .	31
5.1	Photon propagation with $\lambda_e = 30$ cm, $D = 45$ cm, and the light source inside the bubble column. . . . .	36
5.2	Photon propagation with $\lambda_e = 100$ cm, $D = 45$ cm, and the light source inside the bubble column. . . . .	37
5.3	Photon propagation with $\lambda_e = 30$ cm, $D = 100$ cm, and the light source inside the bubble column. . . . .	38
5.4	Photon propagation with $\lambda_e = 30$ cm, $D = 45$ cm, and the light source outside the bubble column. . . . .	39
5.5	Illustration of the simulation and position parameters $r$ and $\phi$ . . . . .	41
5.6	Angular profile of LED XRL-400-5O. . . . .	42
5.7	Detection uniformity of PMT SQ0262. . . . .	43
5.8	$\lambda_e$ and $D$ dependence of NPE. . . . .	44
5.9	$r$ and $\phi$ dependence of NPE. . . . .	45
5.10	Angular profile of the LEDs. . . . .	47
5.11	Cameras in a D-Egg. . . . .	48
5.12	Example of a PDF of NPE. . . . .	49
5.13	Example of the test statistic distribution. . . . .	51
5.14	Example of the PDF of $R$ . . . . .	51
5.15	True scenarios tested. . . . .	52
5.16	Results of likelihood fit tests where $r_{\text{true}}, \phi_{\text{true}}$ are known. . . . .	54
5.17	Results of likelihood fit tests where $r_{\text{true}}, \phi_{\text{true}}$ are unknown. . . . .	55
5.18	P-values for test data from LEDs with +30% of -30% of brightness. . . . .	56
5.19	P-values for test data from LEDs with a different angular profile. . . . .	56
5.20	P-values for test data from three LEDs out of four. . . . .	56
5.21	p-values for test data from $\langle \cos \theta \rangle$ . . . . .	56
5.22	Results of likelihood fit tests where $r_{\text{true}}, \phi_{\text{true}}$ are unknown and the systematic uncertainties are included. . . . .	58

# Chapter 1

## Introduction

The first concrete ideas to search for astrophysical neutrinos were proposed in 1960 by K. Greisen [1]. The first discovery of a PeV-energy astrophysical neutrino flux was made by IceCube in 2013 [2], which opened a new field of astroparticle physics, high-energy neutrino astronomy. Neutrinos are unique messengers that carry information about their parent cosmic ray particles to the Earth without being absorbed or deflected. The most interesting outcome from neutrino astronomy would be the identification of neutrino or cosmic ray sources and elucidation of acceleration mechanisms of cosmic ray particles. In 2018, the IceCube collaboration found evidence of the blazar TXS0506+056 being a cosmic neutrino source, and thus also likely a cosmic ray source [3].

The IceCube Neutrino Observatory is the worlds largest neutrino detector built at the geographical South Pole. The optical modules deployed in the deep ice observe neutrinos by detecting Cherenkov light from charged particles produced in the interactions of neutrinos with the ice. Neutrinos are reconstructed from the amount and timing of the detected light, which relies on the properties of the detection medium. Precise knowledge of the detection medium for very large volume neutrino telescopes is one of the biggest challenges, as the medium is usually in a remote location and not man-made. In IceCube, the optical modules are equipped with light emitting diodes (LEDs) as artificial light sources for measuring the optical properties of the ice. Previous measurements performed in IceCube have measured the properties of the undisturbed glacial ice (bulk ice) [4], while the properties of the re-frozen ice, called “hole ice”, are still inconclusive due to a lack of suitable devices.

The IceCube Upgrade, planned for deployment in the 2022/2023 South Pole Summer, will involve deployment of new optical modules, aimed at

improving the precision of neutrino measurements. One type of new optical module is the “Dual optical sensor in an Ellipsoid Glass for Gen2” (D-Egg). The D-Egg has an improved photon detection efficiency and optimized calibration devices, including LEDs, for measurements of the hole ice properties.

To understand the performance of the calibration devices, a GEANT4 based simulation was performed to parameterize the hole ice system. A maximum likelihood fit was performed to calculate the sensitivity to various hole ice parameters. The results show the D-Egg’s hole ice calibration system has the potential to characterize the hole ice more precisely than in previous measurements. Improved understanding of the hole ice properties will enable the better angular reconstruction of GeV energy neutrinos, which is currently limited by systematic uncertainty of the hole ice properties [5]. Long-term improvements to angular reconstruction and overall reduction of ice modeling systematic errors will greatly benefit all IceCube analyses including neutrino astronomy and cosmic ray source searches.

An overview of IceCube is described in Chapter 2 of this thesis. Chapter 3 describes the D-Egg and Chapter 4 introduces the GEANT4 based D-Egg simulation. Chapter 5 presents the simulation study of hole ice measurement with the D-Eggs and discusses practical considerations. Chapter 6 summarizes this thesis and discusses the scientific reach of this work.

## Chapter 2

# IceCube

### 2.1 Introduction to high-energy neutrino astronomy

High energy primary cosmic rays are believed to be accelerated by astrophysical objects such as supernova remnants, active galactic nuclei and gamma ray bursts, however their origin and the acceleration mechanism is not fully known. Charged cosmic rays are generally composed of protons (90%),  $\alpha$  (9%), and heavier nuclei. Other cosmic rays include gamma-rays and neutrinos. These cosmic rays can be produced up to very high energies, arriving at Earth with up to 100 EeV [6]. By detecting either primary or secondary cosmic rays, IceCube is able to discover more about these extragalactic sources.

In the case of charged primary cosmic rays, they interact with magnetic fields. This is important for two reasons. Firstly, the directions of primary cosmic rays are altered by magnetic fields as they propagate towards the Earth, obscuring their true origins. Secondly, cosmic rays can be confined with magnetic fields at the source. However protons, for example, can collide with ambient matter, which results in another challenge for detecting primary charged cosmic rays.

A common interaction mode for the cosmicly accelerated proton results in either hadronuclear pion production:

$$p + p \rightarrow \pi + X \quad (\pi = \pi^{\pm}, \pi^0) , \quad (2.1)$$

or in photohadronic pion production from interactions with the radiative field in the source region:

$$p + \gamma_{\text{radiation}} \rightarrow \begin{cases} \pi^0 + p \\ \pi^+ + n . \end{cases} \quad (2.2)$$

The pions subsequently decay producing electrons and neutrinos:

$$\pi^0 \rightarrow \gamma\gamma \quad (2.3)$$

$$\begin{aligned} \pi^\pm &\rightarrow \mu^\pm \nu_\mu^{(-)} , & (2.4) \\ \mu^+ &\rightarrow e^+ \bar{\nu}_\mu \nu_e \\ \mu^- &\rightarrow e^- \nu_\mu \bar{\nu}_e . \end{aligned}$$

Each of the three neutrinos produced in the decay of a  $\pi^\pm$  Eq. (2.4) carries approximately  $\frac{1}{20}$  of the energy of the parent proton. In addition to Eq. (2.3), high energy gamma rays can be produced by Inverse Compton scattering. In the regions of strong cosmic magnetic fields, a high density of electrons and photons, produced via synchrotron radiation, react and produce high energy gamma rays:

$$e^- + \gamma_{\text{radiation}} \rightarrow e^- + \gamma_{\text{high energy}} . \quad (2.5)$$

However, these photons acquire energy by Inverse Compton scattering up to 10–100 TeV, but unlikely to PeV-level energies. Observations of PeV gamma rays produced by the reaction in Eq.(2.3), therefore, can be a proof of hadronic acceleration. However, the PeV gamma rays are highly attenuated during propagation by the cosmic microwave background (CMB):

$$\gamma_{\text{PeV}} + \gamma_{\text{CMB}} \rightarrow e^+ + e^- , \quad (2.6)$$

making their detection extremely challenging.

### 2.1.1 High-energy astrophysical neutrinos

Neutrinos are nearly massless leptonic particles with no charge and only interact weakly, meaning they mainly propagate through the universe to the Earth without absorption or deflection. As neutrinos from astrophysical sources can be traced back to their origins, such neutrinos can be used to improve our understanding of charged cosmic rays—their origins and acceleration processes. To compensate for the small interaction probability large volume detectors and high exposure times are required.

## 2.2 The IceCube experiment

The IceCube Neutrino Observatory [7] is a cubic-kilometer neutrino detector built in the South Pole ice between depths of 1450 m and 2450 m, designed to detect GeV–EeV neutrinos. The large volume of transparent,

clear and deep ice is perfect for a neutrino detector. The detector construction was completed on December 18, 2010, and the full operation started in May 2011. IceCube has been primarily aiming to discover high-energy astrophysical neutrinos and identify their sources, in addition to the search for dark matter, the study of neutrino oscillations and the observation of Galactic supernova explosions [8]. The first discovery of high-energy astrophysical neutrinos was achieved in 2013 [2] [9]. In 2018, an origin of the astrophysical neutrinos was identified for the first time, by gamma ray follow-up observations to detect a gamma-ray flare [3].

## 2.2.1 Detector

### 2.2.1.1 IceCube array

The detector array is composed of 5160 digital optical modules (DOMs) across 86 vertical strings, with 60 DOMs on each string. In Figure 2.1 the DOMs are mostly deployed with a vertical spacing of 17 m, and a horizontal of 125 m. This sparse spacing is sufficient due to the long optical attenuation length of the South Pole ice. Eight strings out of 86 at the center of the IceCube array compose a dense sub-array called DeepCore [10], mainly aimed at measurements of neutrinos with energies of 10–100 GeV, and the indirect detection of dark matter. In DeepCore the DOMs are placed below the depth of 2000 m with a vertical separation of 7–10 m and a horizontal separation of 41–105 m.

### 2.2.1.2 DOM—Digital Optical Module

A DOM has a downward-facing 10” photomultiplier tube (PMT) in a pressure-resistant glass sphere with a diameter of 35 cm, along with related circuit boards for processing the PMT pulses and communicating with computers on the ice surface (Figure 2.2). The DOM also contains an LED flasher board for calibration. 12 LEDs are mounted to the edge of the flasher board, divided into six pairs with a  $60^\circ$  separation. One LED in each pair emits light in the horizontal plane and the other  $48^\circ$  above the horizontal, which is close to the Cherenkov angle in the ice. The LEDs were selected to have 399 nm wavelength to match the typical wavelength of Cherenkov photons the DOMs detect. The flasher pulses are programmable and can produce pulses detectable by other DOMs located up to 0.5 km away, making the LEDs useful for various calibration studies. These studies include determining the detector geometry, PMT performance time offset and resolution, and the optical properties of the ice [11].

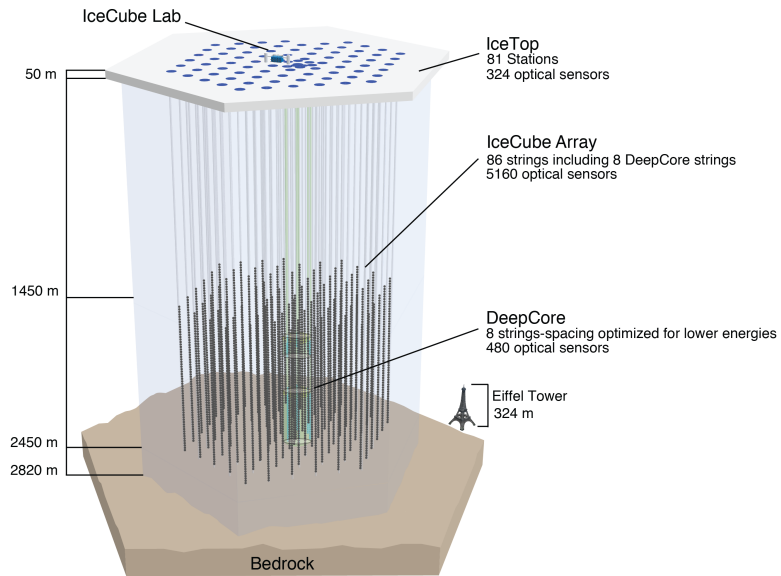


**Figure 2.1:** Sketch of the IceCube detector. The IceCube Laboratory at the surface has the overall detector operation systems, where all the cables connected to the DOMs are gathered.

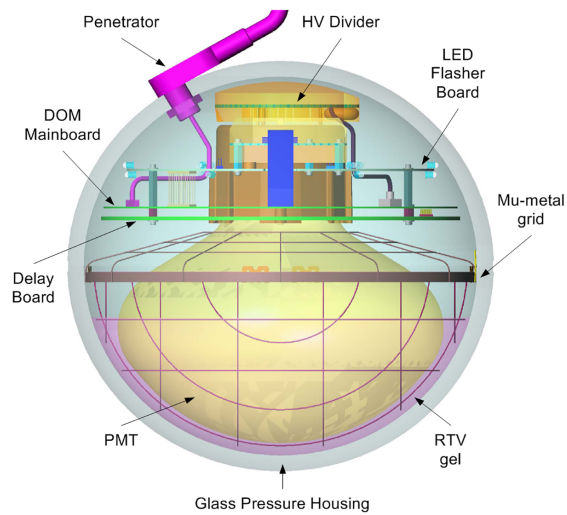


**Figure 2.2:** A schematic of the DOM.

### 2.2.1.3 Construction

In order to build IceCube’s DOM array, 86 boreholes of 2500 m depth in the glacial ice were created. It was achieved by hot water drilling which is more time and fuel efficient than a conventional drill.

The 5 MW Enhanced Hot Water Drill (EHWD) was designed for the IceCube detector construction [12]. The drill head delivers 88°C hot water with a pressure of 7600 kPa. The head was equipped with instrumentation to make a precise hole, such as calipers to measure the hole diameter, a pressure sensor to measure depth, two liquid pendulums to measure tilt relative to vertical, and a fluxgate compass to measure horizontal orientation. The hole diameter was optimized to balance the cost and the rate of water freezing and was decided to be 60 cm.

After the drill was withdrawn from the hole, the hole was filled with water, though the water in contact with the outer ice starts freezing immediately. In order to place 60 DOMs at the planned depth, they were all connected to one cable of 2505 m length with a diameter of 46 mm, together with four 100 pound weights. The water in the hole then freezes the DOMs in place. The ice in the hole created as a result of hot water drilling is called the “hole ice”, discussed in Section 2.2.4.2 and Chapter 5.

## 2.2.2 Neutrino detection principle in IceCube

### 2.2.2.1 Neutrino interactions

Charged-current (CC) neutrino-nucleon interactions produce a lepton  $l = e, \mu, \tau$ :

$$\bar{\nu}_{l}^{(-)} N \rightarrow l^{\mp} X, \quad (2.7)$$

where  $N$  denotes the target nucleon and  $X$  the hadronic final state. The lepton carries an average of 50% to 80% of the neutrino energy depending on the neutrino’s energy, and the remaining energy is transferred to the nucleon. In the case of IceCube, both the lepton and the hadronic shower emit Cherenkov radiation.

Neutral current (NC) neutrino-nucleon interactions do not produce a charged lepton:

$$\bar{\nu}_{l}^{(-)} N \rightarrow \bar{\nu}_{l}^{(-)} X. \quad (2.8)$$

The neutrino transfers a fraction of its energy to the target nucleon, producing a hadronic shower only.

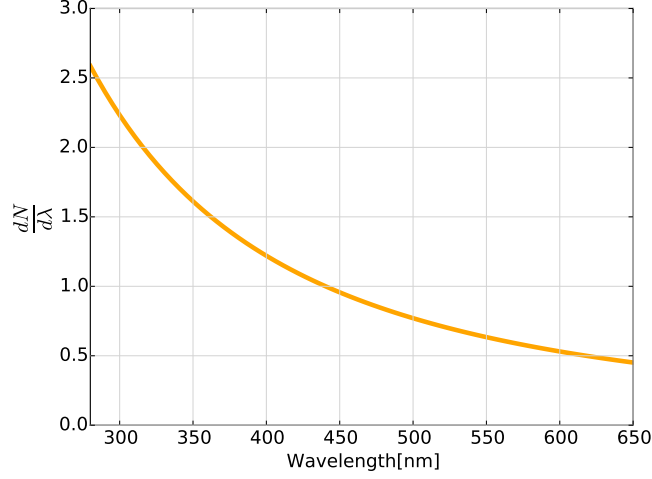


**Figure 2.3:** Cherenkov light yield (Eq. (2.10)) with  $\beta = 1, x = 1$  cm.

### 2.2.2.2 Cherenkov light

When a neutrino interacts with a nucleus in the ice, charged particles are generated (see Eq. (2.7) and (2.8)). When the charged particles move faster than the speed of light in ice, they can travel through the IceCube ice emitting Cherenkov photons, which are detectable by the DOMs near the trajectory of the charged particle.

Photons are emitted at a characteristic angle relative to the charged particle composing the so called “Cherenkov cone”. This characteristic angle is called the Cherenkov angle and is given by

$$\cos \theta_c = \frac{1}{\beta n(\lambda)}, \quad (2.9)$$

where  $\beta$  is the speed of the charged particle in units of the speed of light and  $n(\lambda)$  is the phase refractive index of the medium. In IceCube the refractive index of the ice is  $n(\lambda) = 1.55749 - 1.57988\lambda + 3.99993\lambda^2 - 4.68271\lambda^3 + 2.09354\lambda^4$  [13]. The number of photons emitted per unit length  $x$  for a charged particle with charge  $ze$  is wavelength ( $\lambda$ ) dependent and given by the Frank-Tamm formula:

$$\frac{d^2N}{d\lambda dx} = \frac{2\pi z^2 \alpha}{\lambda^2} \left( 1 - \frac{1}{\beta^2 n^2(\lambda)} \right), \quad (2.10)$$

where  $\alpha = 1/137$  is the fine structure constant (Figure 2.3). IceCube mainly detects photons with a wavelength from 300 to 600 nm.

### 2.2.3 Event types

Three different event topologies are observed in IceCube, depending on the neutrino interaction channel and energy.

#### 2.2.3.1 Track like event

$\nu_\mu$  CC interactions cause track like events. Muons have a long life time such that they can travel through the IceCube detector from end to end, emitting Cherenkov radiation along its trajectory. This enables reconstruction of the muon arrival direction, resulting in an angular resolution to better than  $1^\circ$  for the muon, and hence the incident neutrino with energies above the TeV range [14]. Furthermore, an upward-going track is an unambiguous signature of neutrinos, since no other particle can penetrate the Earth. Therefore, this event type is ideally suited for identification of astrophysical neutrino sources. On the other hand, since the muon track can be too long to be fully contained within the IceCube detector, it is difficult to reconstruct the full energy of the neutrino, coupled with the large background of atmospheric  $\nu_\mu$ .

#### 2.2.3.2 Cascade event

Cascades are formed by particle showers near the neutrino vertex with lengths of order 5–20 m. CC interactions of  $\nu_e$  and  $\nu_\tau$  produce both hadronic and electromagnetic showers. NC interactions of all flavors produce exclusively hadronic showers. The total energy deposited in the detector is proportional to the cascade energy, and thus provides a more direct measurement of the neutrino energy with about 15% accuracy, which is much better than for muon tracks. However, the precision of the angular reconstruction for cascades is worse than for tracks, since the lever arm for fitting the direction is small. Moreover, the strong scattering of photons in the refrozen ice further blurs the original direction information contained in the Cherenkov cone.

#### 2.2.3.3 Double Bang

At PeV energies, the CC interaction of  $\nu_\tau$  cause a third type of event, as the lifetime of  $\tau$  leptons is sufficiently long to travel up to hundreds of meters before decaying. This event is called the double bang, composed of two cascades connected by a rather dim tau track: one cascade is produced when the  $\nu_\tau$  interacts, and the second when the  $\tau$  decays. However, a clear double bang event has not been observed so far.

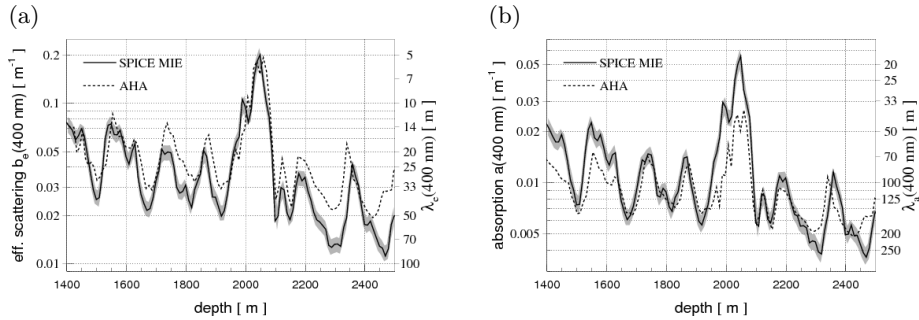


**Figure 2.4:** Depth dependence of the scattering (a) and absorption (b) length at a wavelength of 400 nm taken from [4]. The solid lines show the latest results with estimated uncertainties shown as gray bands.

## 2.2.4 Ice properties

As photons propagate to the DOM's PMT, they are affected by absorption and scattering in the ice. These effects must be implemented into both simulation and reconstruction of IceCube data. The optical properties of the ice have been measured using flasher LEDs in the DOMs.

### 2.2.4.1 Bulk ice

The optical properties of the undisturbed glacial ice (bulk ice) is parameterized by considering the absorption and scattering [4]. To determine the bulk ice parameters, measurements were performed with the IceCube detector. Photons were emitted by the flasher LEDs located inside the DOMs, and the total number of detected photons and the photon arrival times were recorded by other DOMs. The measurement was performed for all depths where DOMs are located, and the wavelength and depth dependence of the scattering and absorption length was determined to be less than 20 m and 5 m, respectively, at 400 nm wavelength (Figure 2.4).

### 2.2.4.2 Hole ice

A camera system, called the Swedish camera, was deployed on one of the 86 strings to monitor how the water in the drill hole refreezes and observe the optical properties of the hole ice. It consists of two rotatable video cameras with LED lamps and four lasers housed in separate glass spheres 5.8 m apart, located at the bottom of the string. The camera images tell the following:

- The water froze from the outside inwards (Figure 2.5(a), 2.5(b), 2.5(c)).

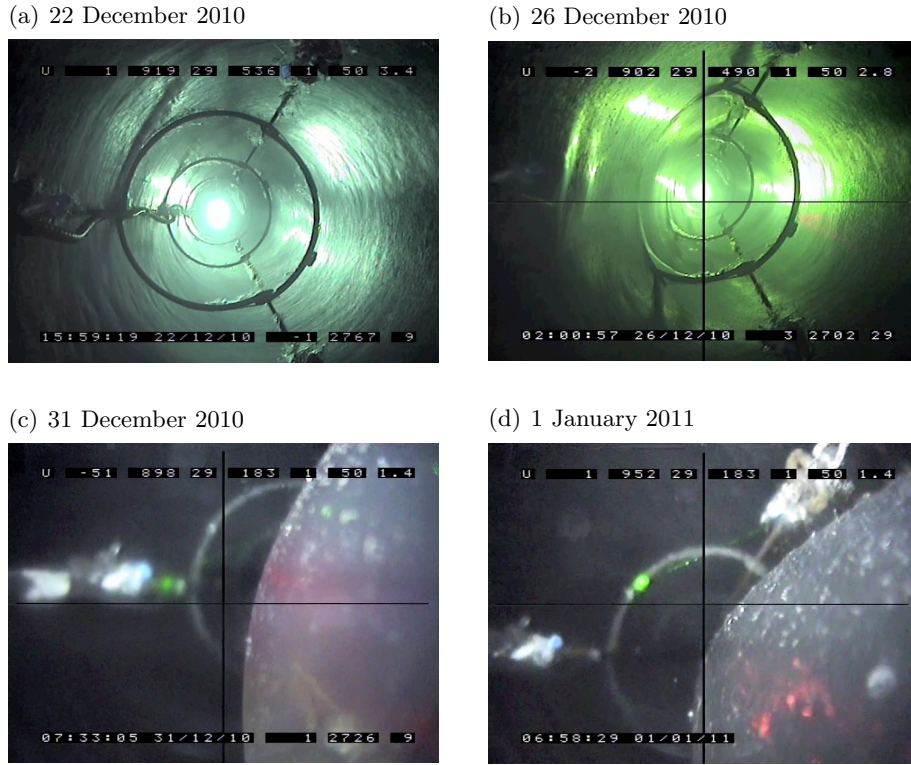


**Figure 2.5:** Hole ice forming images over nine days, 4 days after the deployment. a) The hole still holds a large volume of water, which looks transparent, and the ice wall is clearly identified. The circle ring spacer serves as a landmark in the later images. b) The boundary of the ice and water has moved toward the inner part of the hole. c) The water freezing has evolved so that the boundary of the ice and the water (seen on the right) is observed from the frozen ice. d) The ice of the outer hole is so transparent that the green laser originating from the upper right on the image can reach the spacer.

- The outer region of the hole ice is as clear, or more transparent, than the bulk ice (Figure 2.5(d)).
- A portion of ice includes a lot of impurities in the hole ice (Figure 2.6).

When the water from the drill, containing various impurities such as air bubbles, still-liquid or dust, froze, the impurities condensed into the central area. This resulted in a central ice column with an enhancement of impurities remaining after re-freezing, called the bubble column.

Since the PMT in a DOM faces downward, the increased scattering in the bubble column leads to detection of more photons than expected. Although efforts have been made to measure the precise hole ice properties utilizing



**Figure 2.6:** Camera image looking downward into the established hole ice. The bubble column is found on the center right. It looks opaque because of the Mie scattering of the light on the impurities.

the flasher LEDs [15], the properties of the hole ice are still inconclusive, because the DOM LEDs cannot illuminate the hole ice directly. This leads to one of the largest systematic uncertainties in the angular reconstruction of cascade events.

## 2.3 IceCube Upgrade

The IceCube Upgrade aims to improve the precise measurement of neutrino interactions. The IceCube Upgrade [16] is planned for deployment in the 2022/2023 South Pole Summer, as a stepping stone to the next generation IceCube detector [17]. In the upgrade, an additional 700 new optical modules (OMs) will be deployed together with calibration modules at a depth between 2150 m and 2425 m, across seven new strings inside the DeepCore sub-array (Figure 2.7).

Several types of new OMs have been developed, including the mDOM [18] and the D-Egg [19]. They have an improved overall photon detection efficiency compared with the current IceCube DOM, and will be deployed with a vertical separation of 2.7 m and a horizontal separation of 20 m, which is much denser than the DOMs' spacing in IceCube, even in DeepCore. These will enable even more precise measurement of GeV energy neutrinos. The IceCube Upgrade also targets better understanding of the optical properties of the ice, especially the hole ice. The new OMs hold optimized calibration devices for this purpose, such as vertically illuminating LEDs and cameras.

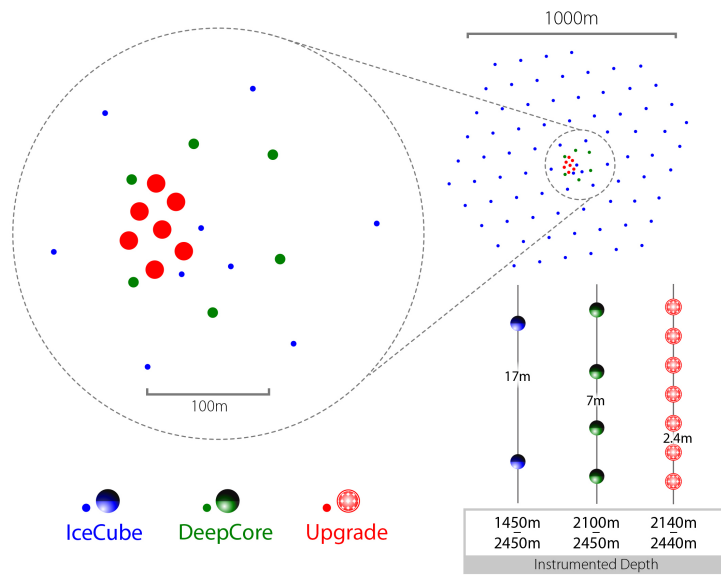


**Figure 2.7:** Sketch of the planned IceCube Upgrade array, including the current DOM spacing for IceCube and DeepCore as well as a zoom towards the DeepCore region, where the narrowly spaced D-Egg and mDOM modules are planned for deployment.

## Chapter 3

# D-Egg

### 3.1 Overview

One type of new optical module for the IceCube Upgrade is called the D-Egg, as seen in Figure 3.1. 300 D-Eggs are planned for deployment as part of the IceCube Upgrade. The D-Egg has a similar structure to the current IceCube DOM, but has been designed to have an improved photon detection efficiency.

The basic idea for the D-Egg is to combine two PMTs for an egg like module. The size of the D-Egg is determined by its glass housing. The housing is composed of two halves each 30 cm in diameter and combine to be 53 cm tall. The upper and the lower sides have an almost symmetrical structure. Both have PMTs as an optical sensor in the pressure-resistant glass hemisphere. A high voltage (HV) board is attached to each PMT, which includes a driver circuit for the PMT and a HV module that increases the input voltage by a factor of 400 to supply to the PMT. Silicone elastomer (gel) between the PMTs and the glass plays a role in fixing the PMT inside the glass and coupling them optically. A magnetic shield made of FINEMET [20] (Hitachi Metals) covers the PMT dynodes avoiding its cathode surface to minimize the impact of the magnetic field on the performance of the PMT.

In addition the lower half has a flasher module, camera module, mainboard and penetrator (Figure 3.2). The flasher and camera modules are installed for the purpose of calibration. The mainboard primarily controls the electronics readout and communication between surface control units and deep ice optical modules through the penetrator. The two half D-Eggs are sealed by vacuuming inside the glass, and then locked in place by a waistband, which has harnesses to hang the D-Egg.

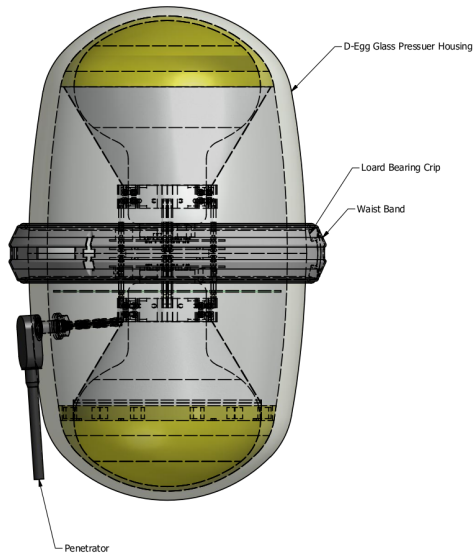


Figure 3.1: Latest prototype of a complete D-Egg.

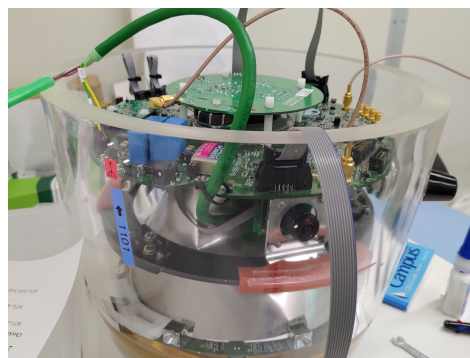
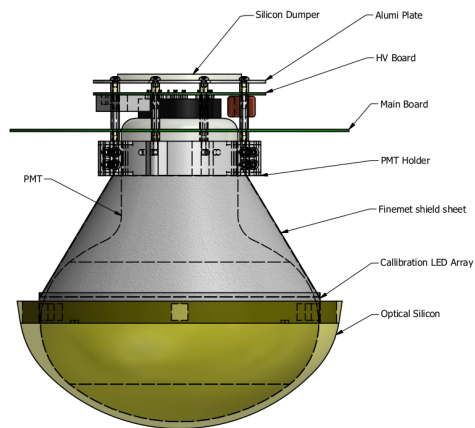


Figure 3.2: Latest prototype of a lower half D-Egg.



**Figure 3.3:** 8” Hamamatsu R5912-100-70 PMT. The yellow hemispherical surface is the photocathode made of bialkali and it is vacuum inside.

## 3.2 PMT

Each D-Egg holds two 8” Hamamatsu PMTs of R5912-100-70 (Figure 3.3).

The photocathode is grounded and a positive voltage is applied to the dynodes by the HV board. When a photon hits the photocathode, it excites an electron on the photocathode surface and emits a photoelectron. This photoelectron has a production probability influenced by the PMT’s quantum efficiency (QE). The intensity of Cherenkov light is higher at shorter wavelengths (see Section 2.2.2), which motivates the selection of PMTs sensitive to 300–650 nm wavelength light and their maximum QE at 350–400 nm (Figure 3.4).

Individual PMTs have unique responses, and several quantities that characterize the PMT response [21] have been measured in the laboratory during the development stage. Before mass-deployment, 10% of the PMTs for the IceCube Upgrade will undergo detailed calibration before being installed into D-Eggs.

### 3.2.1 Gain

A photoelectron generated at the photocathode is collected by the first dynode according to the potential difference. When the photoelectron hits the first dynode, secondary electrons are produced. The secondary electrons are then multiplied when they hit each of the subsequent nine dynodes, and eventually between  $10^6$  and  $10^7$  electrons are collected by the anode to be output, depending on the applied voltage. The electron multiplication factor

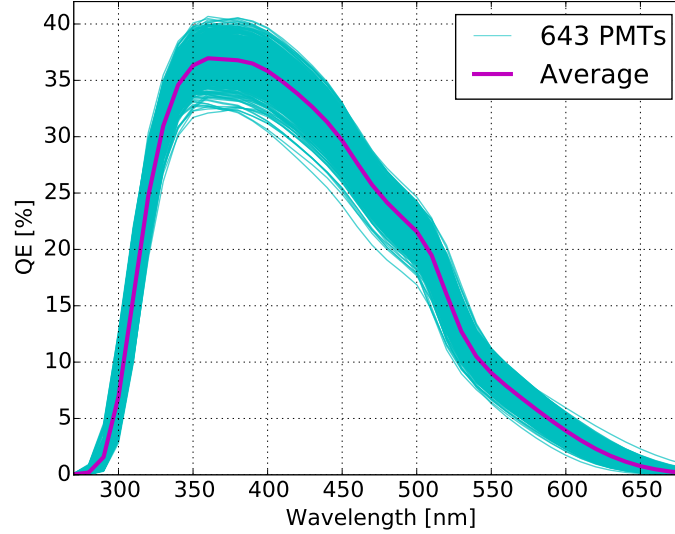


**Figure 3.4:** QE of all PMTs planned for the IceCube Upgrade measured by Hamamatsu. The maximum QE for each PMT is more than 32%.

is called the gain.

The total charge  $Q$  for a given waveform (Figure 3.5) is calculated using:

$$Q = \int dt \frac{V}{R}, \quad (3.1)$$

where  $t$  is time,  $V$  is the voltage, and  $R$  is the impedance, whose nominal value is  $50 \Omega$ .

If we know the gain of the PMT  $G$  for the given supply voltage, the number of photoelectrons (NPE) accepted by the PMT is calculated from the charge of the output signal:

$$\text{NPE} = \frac{Q}{eG}, \quad (3.2)$$

where  $e$  is the elementary charge.

The PMTs are operated at  $G = 10^7$  in IceCube, however we do not know the value of the supply voltage a priori. To determine the supply voltage needed for  $10^7$  gain, a range of supply voltages are applied in the laboratory. In the measurement, 10000 waveforms are recorded for a dim input light with constant intensity, and the charge of each waveform is calculated. Most of the waveforms show no pulse, which constitute pedestal events, while the others mostly are SPE events. The charge distribution is fitted with a function containing nine parameters (Eq. (3.3)). Eq. (3.3) includes a sum of Gaussian functions for pedestal, SPE and two photoelectron (2PE)

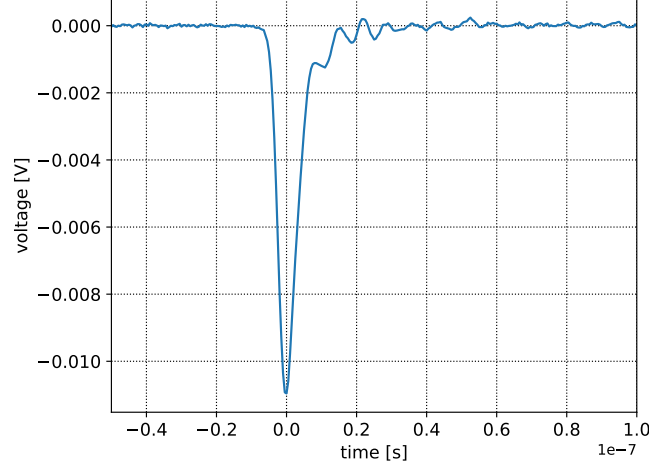


**Figure 3.5:** Example of a waveform when a single photoelectron (SPE) is accepted by the PMT.

events, and an exponential function describing failed multiplication events (Figure 3.6):

$$\begin{aligned}
 f(Q) = & A_{\text{pede}} \exp\left(-\frac{(Q - \mu_{\text{pede}})^2}{2\sigma_{\text{pede}}^2}\right) \\
 & + \frac{1}{2}A_{\text{exp}} \exp(-Q/\tau) \left(1 + \operatorname{erf}\left(\frac{Q}{\sqrt{2}\sigma_{\text{pede}}}\right)\right) \\
 & + A_{\text{SPE}} \exp\left(-\frac{(Q - \mu_{\text{SPE}})^2}{2\sigma_{\text{SPE}}^2}\right) \\
 & + A_{2\text{PE}} \exp\left(-\frac{(Q - 2\mu_{\text{SPE}})^2}{2(\sqrt{2}\sigma_{\text{SPE}})^2}\right),
 \end{aligned} \tag{3.3}$$

where  $A$  is a normalization constant for each component,  $\mu_{\text{pede}}, \sigma_{\text{pede}}$  are the mean charge and the standard deviation for pedestal distribution,  $\mu_{\text{SPE}}, \sigma_{\text{SPE}}$  are the mean charge and the standard deviation for SPE distribution. An example of this combined fit is shown in Figure 3.6 for charge distributions collected from a D-Egg PMT. The various fit parameters are given in the plots where [p0, p1, p2, p3, p4, p5, p6, p7, p8] corresponds to [ $A_{\text{SPE}}, \mu_{\text{SPE}}, \sigma_{\text{SPE}}, A_{2\text{PE}}, A_{\text{pede}}, \mu_{\text{pede}}, \sigma_{\text{pede}}, A_{\text{exp}}, \tau$ ].

The ratio  $\sigma_{\text{SPE}}/\mu_{\text{SPE}}$  is referred to as the charge resolution (Figure 3.7(a)). The ratio of the frequency of observing a charge at the peak of SPE and the valley between the pedestal and the SPE is also a feature quantity of a PMT, called the peak to valley ratio (P/V) (Figure 3.7(b)). This provides

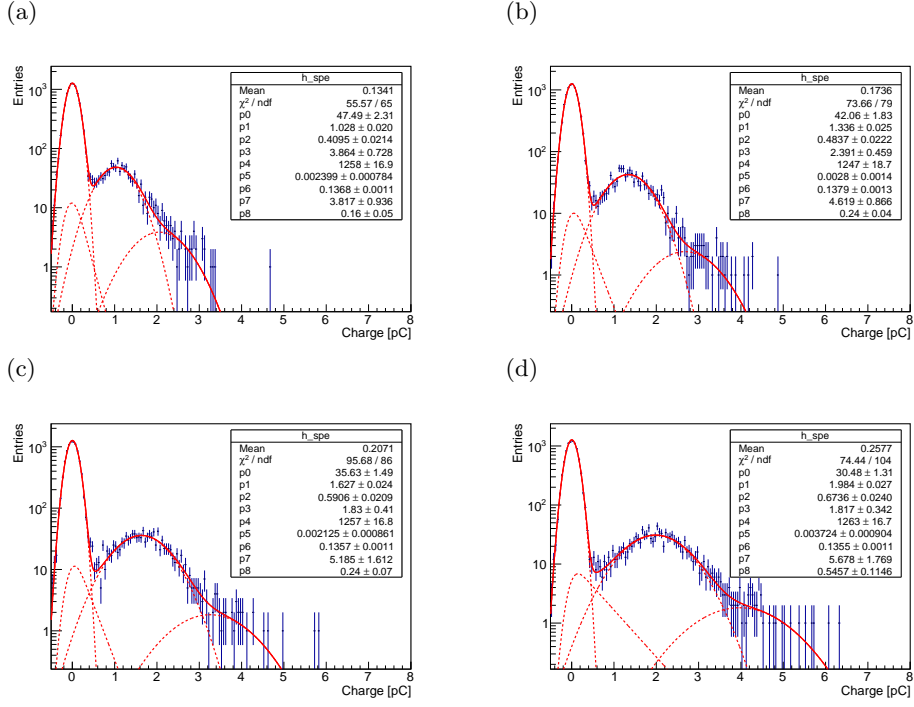


**Figure 3.6:** Example of a PMT's charge distributions for a voltage a) 1440 V, b) 1480 V, c) 1520 V, d) 1560 V. Data are shown as a blue histogram and is fitted with Eq. (3.3) shown as a red solid line. Red dashed lines from left to right correspond to the first, second, third and fourth term of the fitting function, respectively.

an estimate of the PMT's signal to noise performance.

The gain for a given PMT at a known supply voltage is calculated from the SPE mean charge  $\mu_{\text{SPE}}$ :

$$G = \mu_{\text{SPE}}/e . \quad (3.4)$$

After measuring the SPE spectrum at various supply voltages, the voltage  $V$  dependence of the gain is obtained by fitting the data points with two parameters:

$$G(V) = \left( \frac{V}{a_0} \right)^{\frac{1}{10\alpha_1}} . \quad (3.5)$$

For example in Figure 3.8, the supply voltage needed to achieve  $10^7$  gain can be extracted directly from the fit.

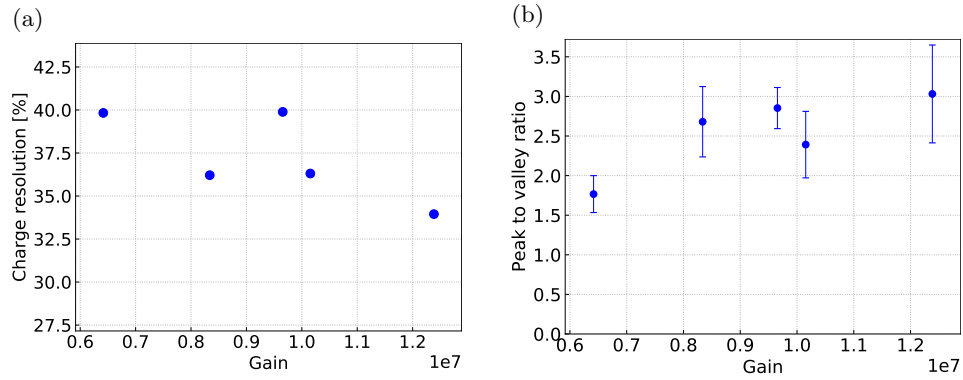


**Figure 3.7:** a) Example of the charge resolution versus the gain. b) Example of the gain dependence of the P/V.

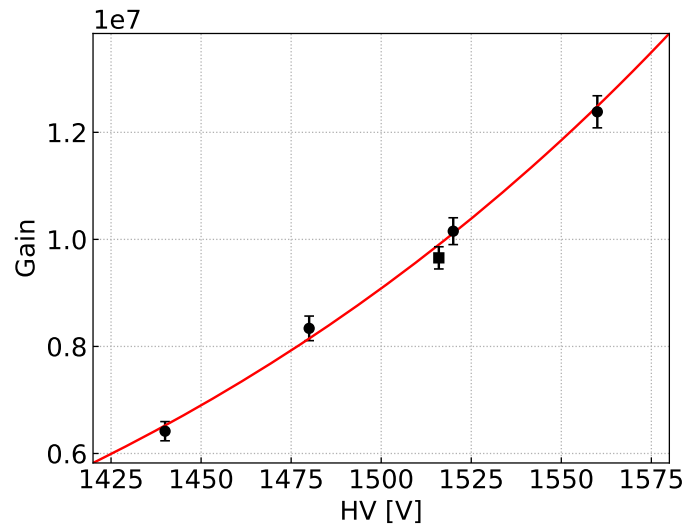


**Figure 3.8:** Example of a gain measurement result, where the gain is plotted as a function of high voltage. The four black circle points are measured data, fitted with Eq. (3.5) shown as a red curve. Once the voltage to achieve  $10^7$  gain is extracted from the fitting function, the gain measurement is repeated for the voltage with more samples (40000 waveforms), shown as the black square.

### 3.2.2 Linearity response curve

The D-Egg PMTs exhibit a linear behavior between the incident amount of light and the output up to several tens of photoelectrons (PEs) over a period of one nanosecond. However, when the PMT detects a huge number of photons within a short time, it saturates and the linearity is lost. In order to estimate the true NPE generated at the photocathode from the output waveform, the linearity of the peak current and NPE is measured in the laboratory from a known input source (Figure 3.9). Waveforms are recorded for six incident lights with different known brightness (Figure 3.9(a)), where the dimmest light is tuned to make a few tens of PEs on the photocathode. The data for the dimmest light is used as an anchor point, assuming it is within the region where the PMT response is perfectly linear. Therefore, the ideal peak current and unsaturated NPE are calculated. Particularly, the ideal current is written as a function of the actual peak current  $x$  using three parameters  $p_0, p_1, p_2$ :

$$f(x) = \frac{1}{\frac{1}{x} + \frac{1}{p_0} \ln \left( 1 + \left( \frac{x}{p_1} \right)^3 \right) / \ln \left( 1 + \left( \frac{x}{p_2} \right)^{\frac{1}{2}} \right)} \quad (3.6)$$

### 3.2.3 Detection uniformity

The probability that a photoelectron is multiplied at each dynode depends on the electrons' trajectory. This is called the collection efficiency (CE). It largely depends on the incident photon interaction point on the photocathode. However, the CE cannot be measured directly, since the position dependence of the QE cannot be separated in the measurement. If assuming the QE is uniform over the photocathode, the CE is obtained by just scaling the measured photon detection efficiency. In the laboratory, a movable light source (Figure 3.10) enables the measurement of the photon detection efficiency in 2D with respect to the incident position of the light source (Figure 3.11). The overall performance of the PMT is referred to as the detection uniformity.

### 3.2.4 Darknoise rate

Even if no light is around the PMT, radioactive decays in the PMT glass or elsewhere can generate an SPE which is detected in the PMT. This is called darknoise. Such PEs can limit the overall sensitivity of a PMT to SPE events and are therefore important to understand. However, because

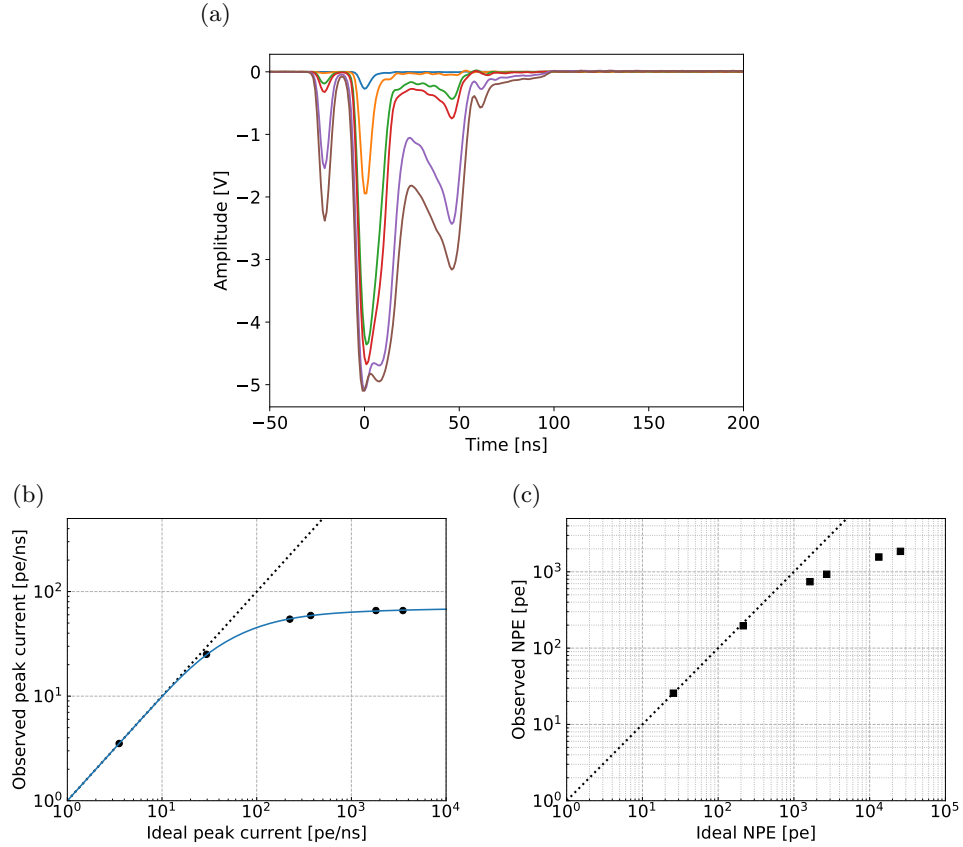


**Figure 3.9:** Example of the linearity measurement results. a) Average waveforms for various input light source intensities. Colors correspond to the input intensities brightness in the order of brown, purple, red, green, orange, blue. Notice how the PMT waveform becomes distorted as the intensity increases. b) The peak of the observed current versus the ideal peak current. The data are fitted with Eq. (3.6) shown as the blue line. Note the departure from the linear region as the ideal peak current increases. c) Number of total PEs detected versus input. This also demonstrates the linear and non-linear regions.

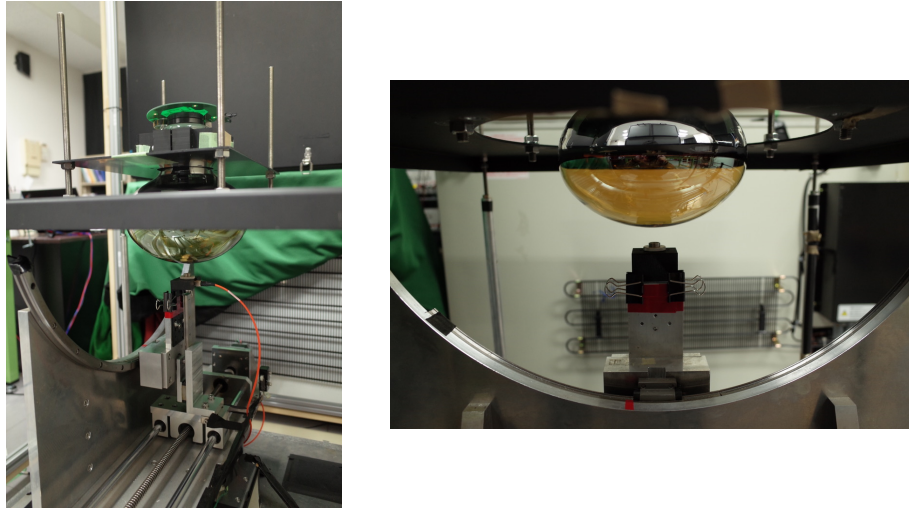


**Figure 3.10:** 2D uniformity measurement setup. The light source output moves along the curve of the metal semi-circle and rotates to fully sample the PMT surface.

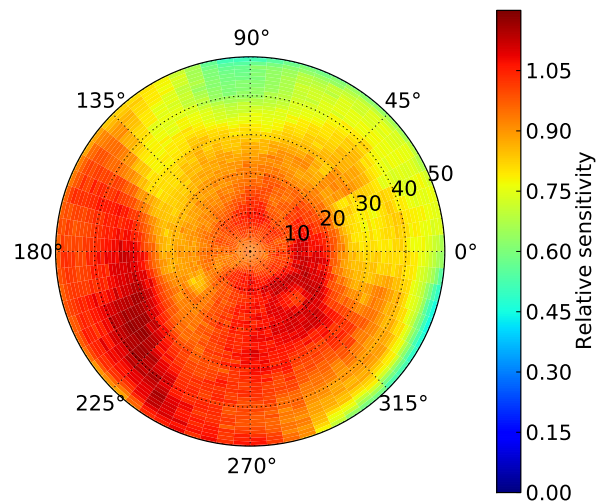


**Figure 3.11:** Example of the detection uniformity of a PMT. The relative sensitivity can be referred to as CE, given that the QE is uniform over the photocathode.

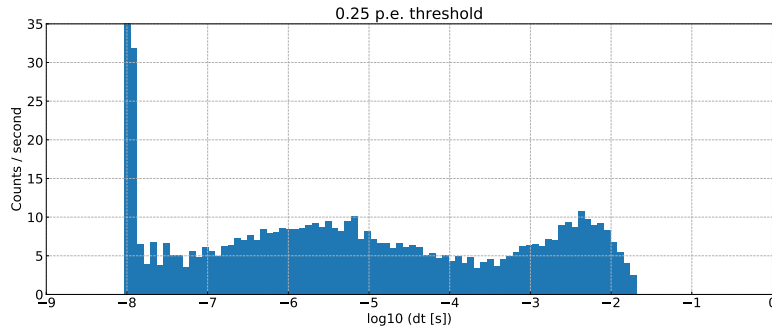


**Figure 3.12:** Example of a darknoise measurement result. The distribution of time intervals,  $dt$ , between peaks exceeding a 0.25 PE threshold when no light source is present is shown here. This measurement is not sensitive to below  $dt = 10^{-8}$ s and above  $dt = 10^{-3}$ s. This is due to resolution and time window limitations in the measurement, respectively.

radioactivity is largely an irreducible background, it is important to characterize these events through laboratory measurements. In the laboratory, the rate of the darknoise is measured under the temperature of  $-30^{\circ}\text{C}$  so as to duplicate the situation where the D-Egg will be deployed (Figure 3.12). At cold temperatures electronics noise is also reduced.

### 3.3 Glass and gel

The glass houses the components, protecting them from the pressure in the deep water or glacial ice. The gel fills the gap between the PMT and glass so that the PMT sticks to the glass and, moreover, is optically coupled to the glass. Both the glass and gel have been developed to have a high transmittance of ultraviolet light, since the Cherenkov radiation intensity is inversely proportional to the emission wavelength. This was achieved mainly by reducing the thickness and selecting more transmissive materials.

The thickness must balance both the photon transparency and the mechanical strength. The glass is 10 mm thick at the top or bottom, which is thinner than the 12.7 mm DOM's glass. The gel is 5 mm thick at the top or bottom, which is half the thickness of the DOM's gel, and 70 mm deep, which covers almost the entire photocathode of the PMT. As a result of the optimization of the thickness and the material, the transmittance is significantly improved compared with the IceCube DOM (Figure 3.13).

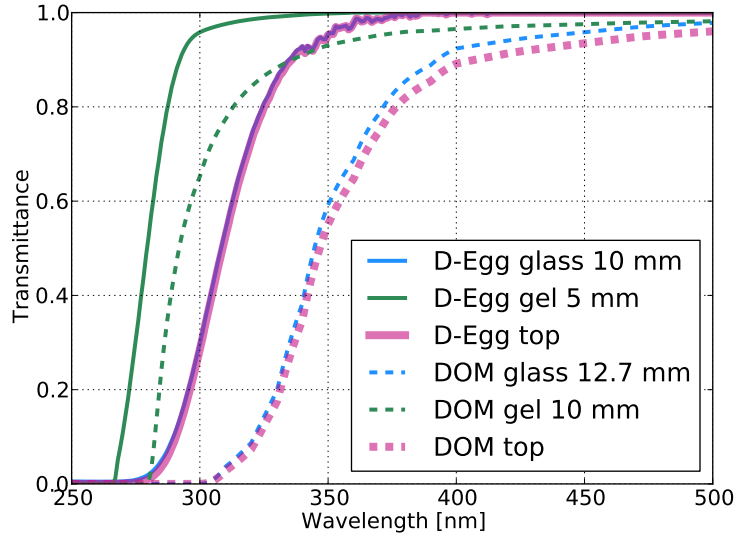


**Figure 3.13:** Transmittance of the glass and gel of the D-Egg compared with the DOM.

### 3.4 Flasher

The D-Egg includes 12 LEDs for calibration purpose (Figure 3.14). All LEDs are mounted to a printed circuit assembly board and are inserted into a special rectangular cup to fix their orientation relative to the D-Egg. These LEDs and the circuit board constitute the “flasher”, which is made to surround the PMT on the gel surface of the lower half D-Egg. XRL-400-50 [22] has been selected as the LED for the IceCube Upgrade flashers. It has a  $15^\circ$  viewing angle and peak wavelength at 400–410 nm.

Eight of the 12 LEDs are pointing in the horizontal plane, mounted on the flasher board with a  $45^\circ$  interval so that they can emit light in all directions. They will be used to calibrate the orientation of the optical modules, as is done currently in IceCube (see Section 2.2.1.2).

The other four LEDs are pointing downward and will be used to calibrate the hole ice properties. Although the IceCube DOM also has flasher LEDs for measuring the optical properties of the ice, they are all horizontal or tilted by  $45^\circ$ , not fully vertical. As such, they are not ideal to measure the hole ice properties. The D-Egg with the fully vertical LEDs has potential to perform more direct hole ice measurements.

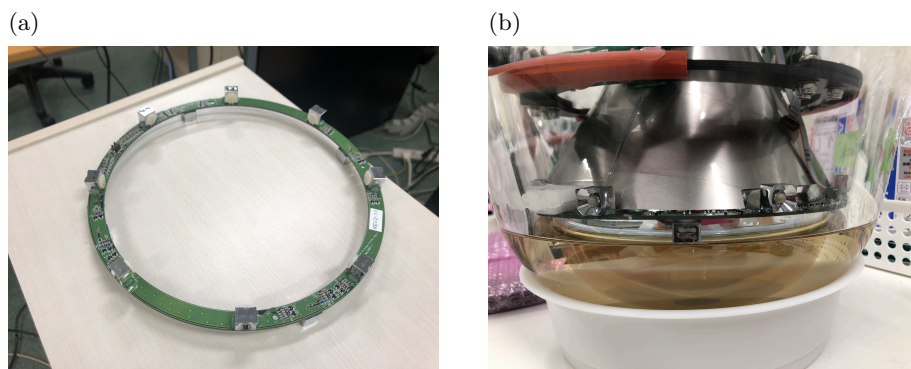


**Figure 3.14:** a) Prototype of the flasher module. b) Flasher module on the gel of the lower half D-Egg, surrounding the PMT.

## Chapter 4

# Detector simulation

### 4.1 DOMINANT

The development of a new detector benefits greatly from a detailed detector simulation. This was also the case for the D-Egg, including understanding how photons interactions in the ice propagate to the PMT. Such an understanding is needed to reconstruct neutrino properties from data taken by the PMTs in each OM. In order to understand the photon absorption, reflection and refraction inside the D-Egg including the glass, a precise D-Egg simulator was developed, inheriting the DOM simulator called DOMINANT [23].

DOMINANT is an IceCube internal full Monte-Carlo simulator based on GEANT4 [24], which traces a photon path directly to the photocathode, including the optical processes of absorption, reflection and refraction.

### 4.2 DOMINANT for D-Egg

The DOM in DOMINANT has been replaced with the D-Egg, changing the geometry based on Figure 4.1, and the optical properties of the glass and gel (see Section 3.3). Note that adding even more detail such as surrounding ice with different properties and the cables which D-Eggs are hung is also possible.

### 4.3 Effective area calculation

The primary purpose of DOMINANT is to derive the effective area of the detector. The DOMINANT simulation allows to access the information of photons when they arrive at the photocathode. After the photons hit

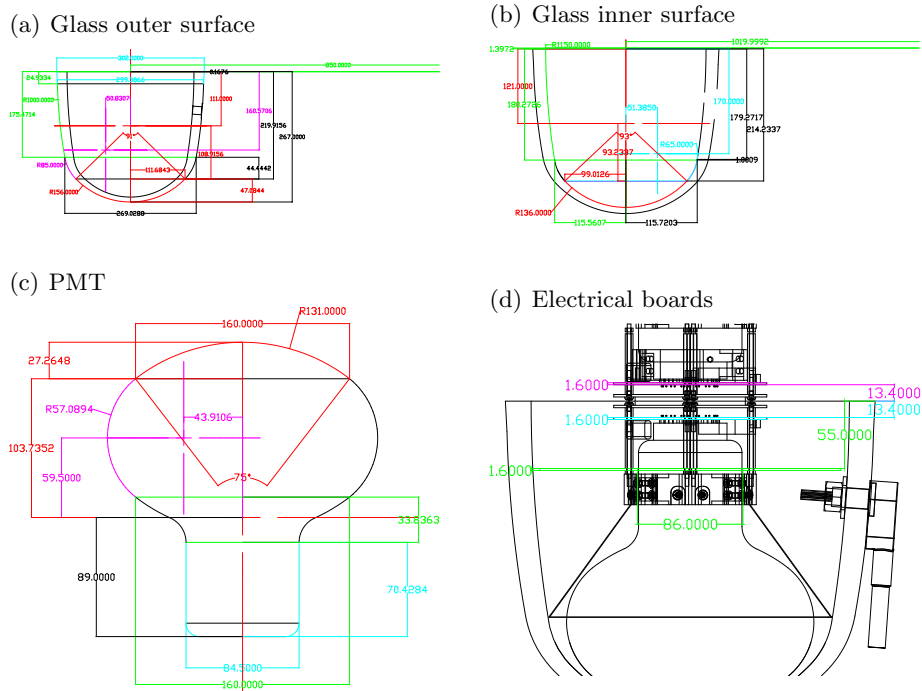


**Figure 4.1:** Designs and geometries of the D-Egg implemented into DOMINANT. The D-Egg solid is modeled as an ensemble of parts of simple shapes such as a cylinder, sphere, and torus.

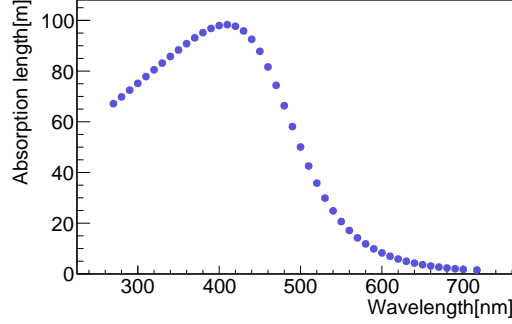


**Figure 4.2:** Wavelength dependence of the absorption length of the bulk ice.

the photocathode, DOMINANT does not trace them any more, however, the PMT response is taken into account in the effective area estimation to conclude more realistic detector performance. The effective area of the D-Egg was calculated from simulations incorporating the measured PMT responses, QE and uniformity.

The zenith angle dependence of the effective area of D-Egg is calculated by placing it in a large volume of bulk ice with a wavelength dependent absorption length (Figure 4.2). A circular parallel beam with a radius  $R_{\text{beam}}$  equal to half the D-Egg height (26.7 cm) consisting of 1000 photons is injected from 35 cm away from the center of the D-Egg, aiming at the center of the D-Egg with a zenith angle  $\theta$  from  $0^\circ$  to  $180^\circ$  (Figure 4.3). The effect of the photon absorption is negligible since the distance from the incident position to the surface of the D-Egg is much shorter than the absorption length of the bulk ice (Figure 4.2).

The probability that a photon generates a photoelectron at the photocathode and is then collected at the PMT dynode can be calculated from several factors measured in the laboratory (see Section 3.2). The probability depends on the photon hit position on the photocathodes, which is recorded in the simulation. For a given PMT, the photoelectron detection probability  $P_{\text{NPE}}$  to the input from zenith angle  $\theta$  is calculated by

$$P_{\text{NPE}}(\theta) = \frac{\sum_{i=0}^{N_{\text{hit}}(\theta)} \text{QE} \times \text{CE}(\mathbf{r}_i(\theta))}{N_{\text{beam}}}, \quad (4.1)$$

where  $N_{\text{hit}}$  is the number of photons that arrive at the photocathode,  $N_{\text{beam}}$  is the number of simulated photons and  $\mathbf{r}_i$  is the  $i$ th hit photon's position on the photocathode.

The effective area  $A_{\text{eff}}$ , including the PMT response, is then calculated

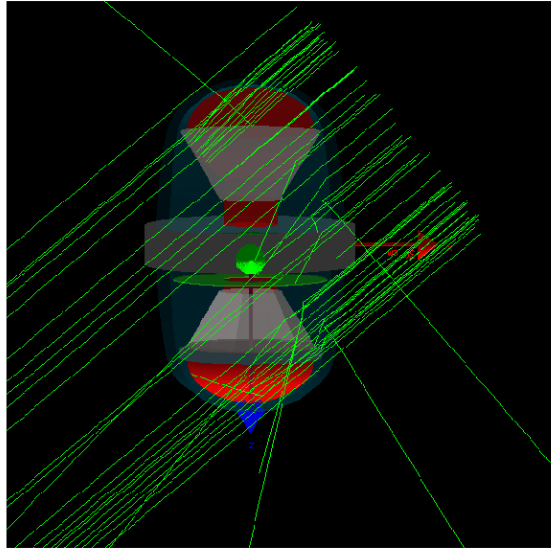


**Figure 4.3:** Depiction of the simulation. Green lines show the photons paths injected from the upper right. Photons are reflected or refracted at the boundary of different materials such as the glass and the surrounding ice. Photon tracing is terminated after the step where the photon enters the PMT from the photocathode surface.

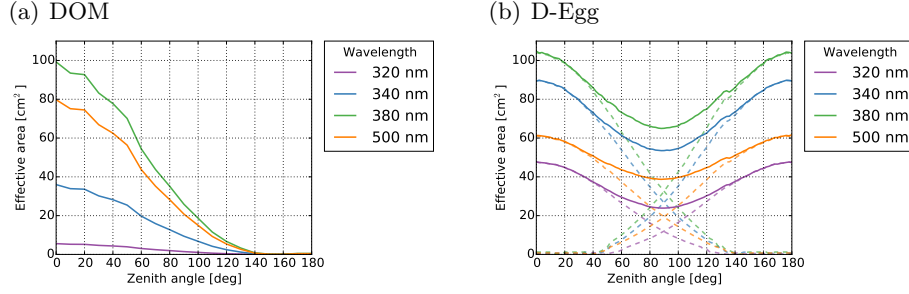


**Figure 4.4:** Zenith angle dependence of the effective area of the DOM (a) and the D-Egg (b). Zenith angle is  $0^\circ$  when the beam aims at the module from the bottom. This study includes a narrow wavelength simulation of photons at 320, 340, 380, and 500 nm as denoted by their colors. a) The effective area is the largest at a zenith angle of  $0^\circ$  since the DOM’s PMT faces downward. The effective area is small for low wavelengths due to the low transparency of the glass. b) The dashed lines show the contribution from each of the upper and lower PMTs, while the solid line is a summation of the two components. At small zenith angles the lower PMT contributes most strongly and at large zenith angles from the upper PMT. The sum of the two PMTs is shown as the solid lines. Performance of the D-Egg is greatly enhanced at lower wavelengths due to increased attention during development of the glass and gel. The D-Egg performance is worse at 500 nm, which is contributed from the geometrical area of the PMTs, although the transmittance of the glass and gel and the QE are still better for the D-Egg than for the DOM.

from the averaged multiple photoelectrons over the input beam area,

$$A_{\text{eff}}(\theta) = P_{\text{NPE}}(\theta) \cdot A_{\text{beam}} , \quad (4.2)$$

where  $A_{\text{beam}} = \pi R_{\text{beam}}^2$  is the area of the beam. As long as  $R_{\text{beam}} \geq 26.7$  cm, the effective area is always obtained to be the same. The zenith angle dependence of the effective area for various wavelengths is shown in Figure 4.4 in comparison with the standard IceCube DOM. The D-Egg is twice or more as sensitive to light from the side as the DOM, and it has the same sensitivity to light from top as bottom, while the DOM is not sensitive to light from the bottom. Additionally, higher PMT QE, more transparent glass and gel optimized for low wavelengths, results in an overall larger effective area for the D-Eggs even from the top or bottom where almost no photon is detected by the PMT facing the other side. This is despite the geometrical area of the D-Egg’s 8” PMT being smaller than DOM’s 10”.

## Chapter 5

# Sensitivity to the hole ice

### 5.1 Introduction

The re-frozen ice in the drill holes, called “hole ice”, has different optical properties from that of the bulk ice (see Section 2.2.4). The bulk ice has  $\sim 20$  m long scattering length for optical light [4], while the hole ice has a much shorter scattering length. The hole ice is composed of two regions: a central column containing some amount of impurities, called the bubble column, and a clear outer region. Impurities in the bubble column serve as targets of Mie scattering for optical photons. Therefore, the properties of the hole ice can be characterized by two parameters; scattering in the bubble column and the bubble column size. Current IceCube DOMs do not have fully vertical LEDs, which are not optimal for directly measuring the hole ice properties. Combined with the large spaces between DOMs (17 m vertically, 125 m horizontally), previous measurements of the hole ice properties remain inconclusive. The lack of understanding regarding the hole ice properties is a dominant source of uncertainties to the directional reconstruction for all neutrinos, and is particularly relevant for  $\nu_e$ ,  $\nu_\tau$ , and neutral current interactions in the GeV region.

As described in Section 3.4, the D-Egg has four LEDs useful for the hole ice measurement. The light emitted by the downward-facing LEDs will then be detected by the D-Eggs in the same hole. Because the optical properties of the hole ice largely depend on the size of the bubble column and the position of the D-Egg relative to the center, using all four LEDs can reduce the overall uncertainty of the hole ice properties. Specifically, measurements with the D-Eggs will determine the bubble column diameter  $D$  and the effective scattering length of the bubble column  $\lambda_e$ . Although D-Eggs will only be deployed in future IceCube expansions, the entire IceCube data

taken since 2011 can be reanalyzed using the updated hole ice parameters.

## 5.2 Simulation of photon propagation in ice

### 5.2.1 Modeling hole ice

To achieve the precise hole ice property measurement that can extract the bubble column diameter  $D$  and the effective scattering length of the bubble column  $\lambda_e$ , the hole ice model includes the bubble column and the clear outer region, as observed by the Swedish camera. A simple situation is considered in this study.

- The drill hole is a perfectly vertical cylinder with a diameter of 60 cm.
- The bubble column is also a perfectly vertical cylinder at the center of the hole.
- Photons undergo Mie scattering only in the bubble column.
- The bulk ice does not scatter photons at all.
- The hole ice outside the bubble column has the same optical property as the bulk ice; the hole ice does not scatter photons at all and there is no optical boundary between them.
- The absorption length is the same for all ice as for the bulk ice (Figure 4.2).

### 5.2.2 Modeling of Mie scattering

The Mie scattering in the bubble column is implemented through the Henyey-Greenstein (HG) scattering function [25], a common approximation and easy to introduce to the Monte Carlo simulation. In the HG approximation, Mie scattering is parameterized by an average scattering angle of  $\langle \cos \theta \rangle$  and a geometrical scattering length  $\lambda_s$ , the average distance between scatters. The scattering angle  $\theta$  follows the normalized density function:

$$p(\cos \theta) = \frac{1 - \langle \cos \theta \rangle^2}{2 \langle \cos \theta \rangle} \left( \frac{1}{1 + \langle \cos \theta \rangle^2 - 2 \langle \cos \theta \rangle \cos \theta} - \frac{1}{1 + \langle \cos \theta \rangle} \right). \quad (5.1)$$

In this study  $\langle \cos \theta \rangle = 0.95$  was chosen since it is comparable to what was used in the study of bulk ice properties [26]. The sensitivity of the result to the value of  $\langle \cos \theta \rangle$  was studied as a part of systematics (see Section 5.5.4). Mie scattering exhibits strongly forward peaked anisotropic scatters, which

means the effective scattering length  $\lambda_e$  is much greater than the geometrical scattering length  $\lambda_s$ . In general, the average cosine of the direction after the  $i$ th scattering  $\langle \cos \theta \rangle_i$  can be expressed as a power of scattering times:

$$\langle \cos \theta \rangle_i = \langle \cos \theta \rangle^i . \quad (5.2)$$

As  $0 < \langle \cos \theta \rangle < 1$ , the average transport distance of photons experiencing the Mie scattering  $n$  times is approximately obtained by

$$\lambda_e = \lambda_s \sum_{i=0}^n \langle \cos \theta \rangle^i . \quad (5.3)$$

Therefore, by taking the limit as  $n \rightarrow \infty$ , the effective scattering length is defined as

$$\lambda_e = \lambda_s / (1 - \langle \cos \theta \rangle) . \quad (5.4)$$

The scattering in the bubble column is now parameterized by only one variable,  $\lambda_e$ .

### 5.2.3 Toy simulation

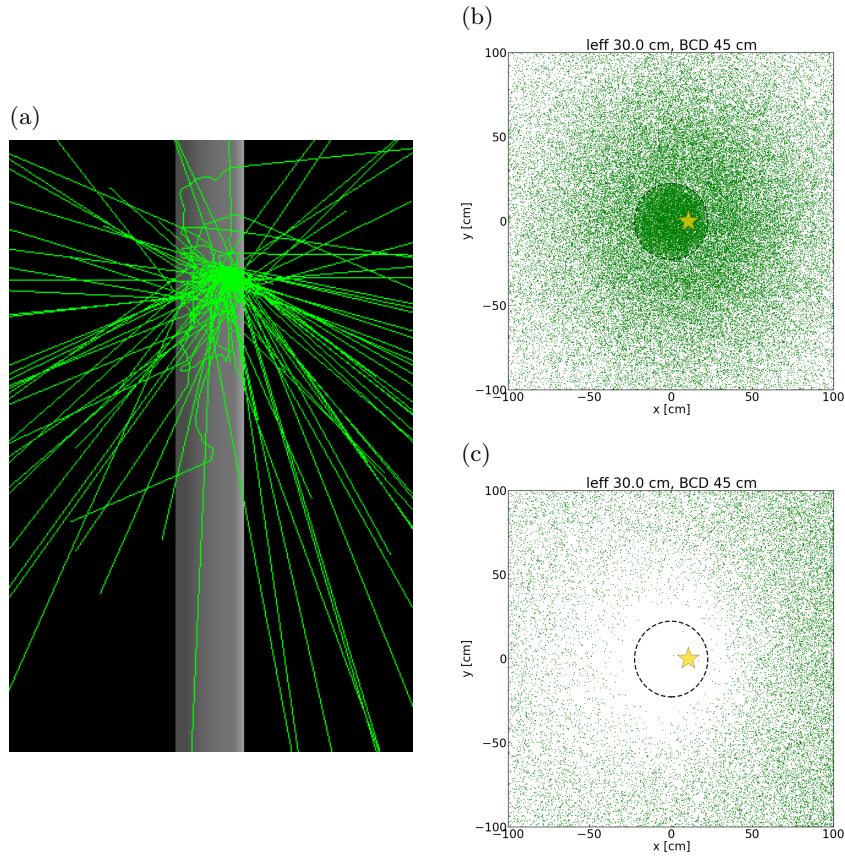
To verify the configuration described above, simple simulations of photon propagation in the ice were performed using GEANT4. Figure 5.1–5.4 show the photon propagation and the position of photons after propagating upwards and downwards, for different scenarios. These scenarios include variations in the scattering length  $\lambda_e$ , bubble column size  $D$  and position of a light source. In Figure 5.1,  $\lambda_e = 30$  cm,  $D = 45$  cm, and the light source is inside the bubble column.

Figure 5.2 considers a longer scattering length than Figure 5.1. Comparing Figure 5.2(b) with Figure 5.1(b), the longer the scattering length, the fewer photons reach the upper plane. On the contrary, a comparison of Figure 5.2(c) with Figure 5.1(c) shows that the longer the scattering length, the more photons reach the lower plane. This is because photons must be scattered to reach the upper plane, while less scattered photons arrive on the lower plane. A long scattering length makes photons less scattered on average, and it results in fewer photons going upward and more photons going downward.

Figure 5.3 illustrates the results for a thicker bubble column than used in Figure 5.1. Comparing Figure 5.3(b) with Figure 5.1(b), and Figure 5.3(c) with Figure 5.1(c), the thicker the bubble column, the more photons reach both the upper and the lower planes. In this case the thick bubble column

provides a field where photons undergo scattering, trapping the photons inside. If a photon escapes, the infinitely long scattering length in the outside ice ensures no photons re-enter in this model.

In Figure 5.4, the light source is located outside the bubble column, unlike Figure 5.1. Comparing Figure 5.4(b) with Figure 5.1(b), fewer photons reach the upper plane when the light source is outside the bubble column than inside, because photons have a low chance to enter the bubble column and then undergo scattering. Photons that are not scattered directly go downward, which makes the area dense with photons as seen in Figure 5.4(c).



**Figure 5.1:** Photon propagation with  $\lambda_e = 30$  cm,  $D = 45$  cm, and the light source inside the bubble column. a) Depiction of the simulation: gray column at the center represents bubble column and green lines show tracks of 100 photons emitted from the light source on the upper right in a  $120^\circ$  downward viewing angle. b, c) Green dots show the hit position of photons on the horizontal plane at 180.5 mm above the light source (b) and at 2433 mm below (c), when  $10^6$  photons are emitted at a wavelength of 405 nm. The positions of the upper and lower planes correspond to the upper PMT of the D-Egg which has an LED at the position of the light source and the upper PMT of the D-Egg 2.7 m below the D-Egg. The yellow star represents the position of the light source, and the black dashed circle represents the bubble column edge.

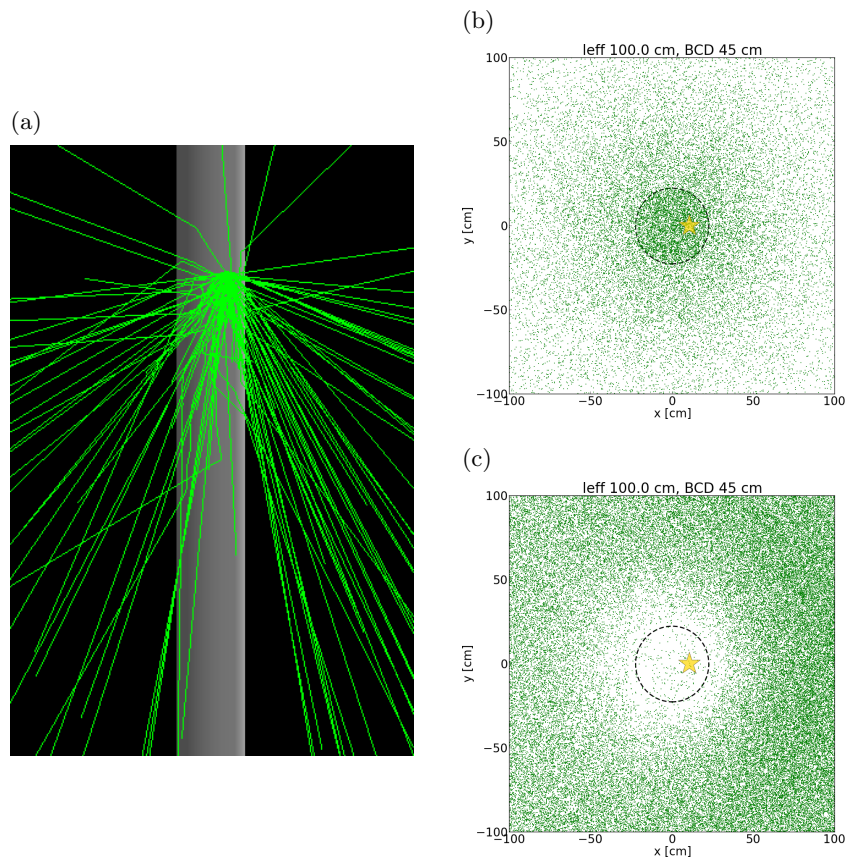


**Figure 5.2:** Same as Figure 5.1, but with  $\lambda_e = 100$  cm.

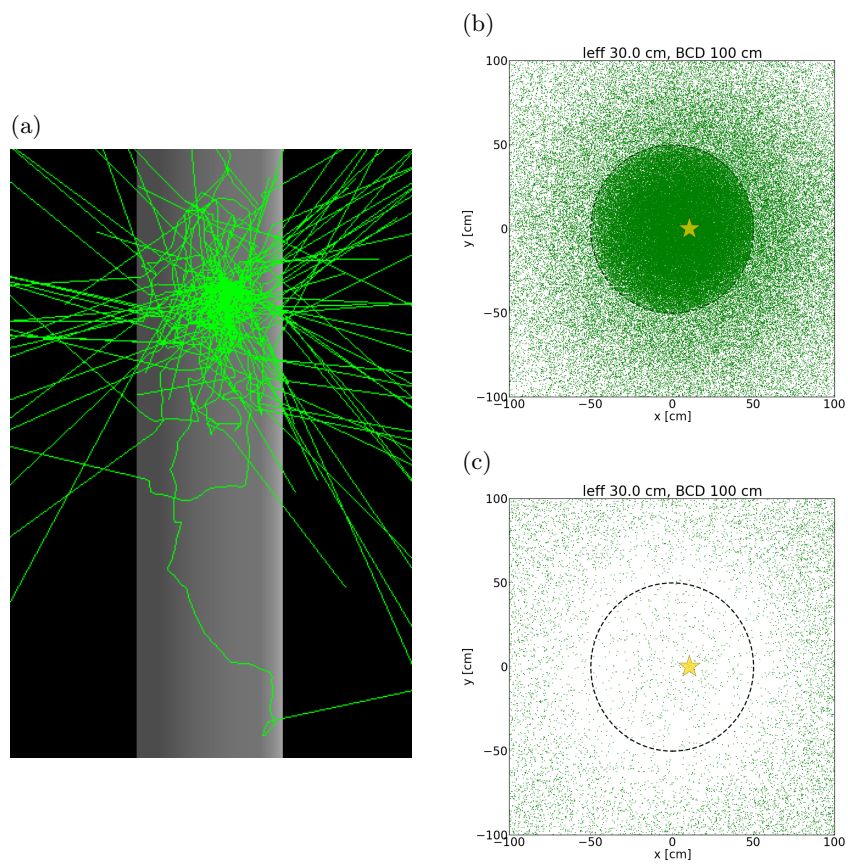
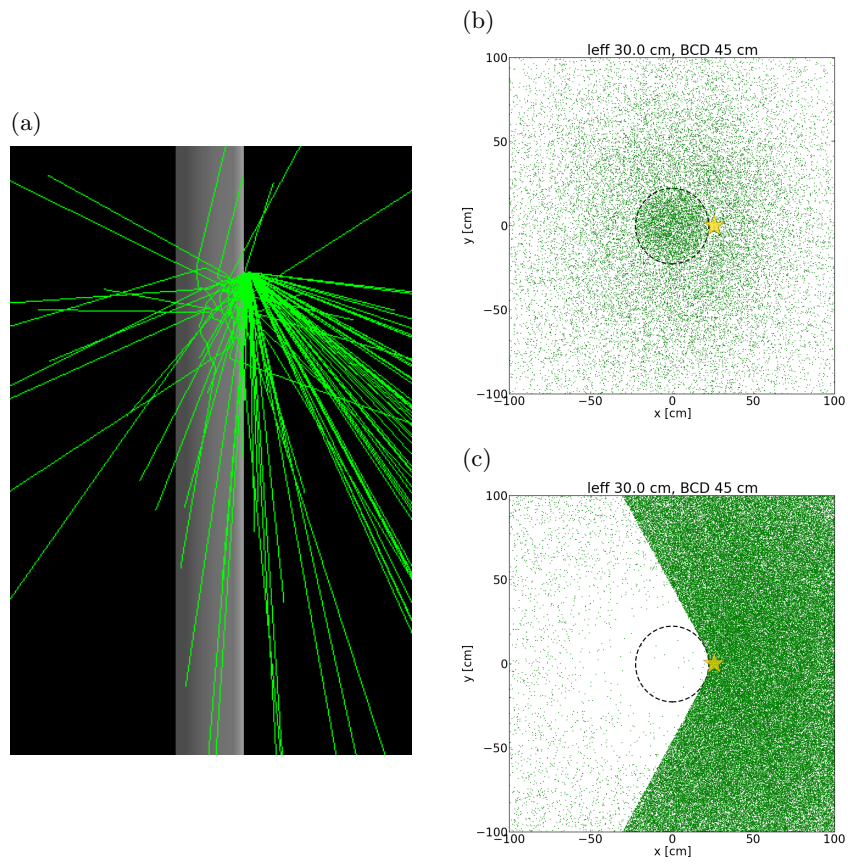


Figure 5.3: Same as Figure 5.1, but with  $D = 100$  cm.



**Figure 5.4:** Same as Figure 5.1, but with the light source outside the bubble column.

## 5.2.4 Photon detection with D-Egg

### 5.2.4.1 Simulation framework

DOMINANT has been expanded so that the performance of hole ice measurements with D-Eggs can be evaluated. As in Section 5.2.3, in the large volume of bulk ice, the 60 cm diameter hole ice including the bubble column with a diameter of  $D$  is generated, as modeled in Section 5.2.1. Two D-Egg modules are simulated perfectly aligned in the 60 cm diameter hole ice with a vertical spacing of 2.7 m. The relative position of the D-Eggs to the center axis of the bubble column is characterized by the distance  $r$  from the bubble column center to the center of the D-Egg module and the rotation around the bubble column center  $\phi$  (Figure 5.5(b)).

When the downward-pointing LED flashes, two different PMTs detect the photons. Both the upward-facing PMT in the lower D-Egg (forward PMT) and the upward-facing PMT in the D-Egg from which the photons originate (backward PMT) can receive these photons (Figure 5.5(a)). But the way in which the photons arrive to the PMTs are very different. This depends primarily on the scattering processes the photons undergo as seen in Section 5.2.3.

However, inaccuracy in calibration of the absolute LED intensity would lead to a large uncertainty in the measurements of amount of light. To minimize the effect of the variation in absolute LED intensity, the ratio of the amount of light detected at the forward PMT and the backward PMT is treated as an observable in this study. Although taking the ratio reduces the information from the measurement, the ratio is still sensitive to the hole ice properties, as the hole ice property dependence of the amount of detected light are different for these two PMTs.

Multiple different setups were simulated with regards to the bubble column effective scattering length, the size of the bubble column, and the position of the D-Egg modules. This was done to investigate the effects of  $\lambda_s$ ,  $D$ ,  $r$  and  $\phi$  over a large range of values.

### 5.2.4.2 Light source

Each of the D-Egg flasher LEDs is capable of producing a pulse with a width less than about 8 ns including  $1 \times 10^6$  to  $1 \times 10^9$  photons/flash, with a peak wavelength at 400–410 nm. The LEDs have an  $15^\circ$  viewing angle with a dip at the center of the angular profile as shown in Figure 5.6.

In this simulation, the downward-pointing LED produces  $2 \times 10^7$  photons and no timing information is used. The LED is modeled as a dimensionless

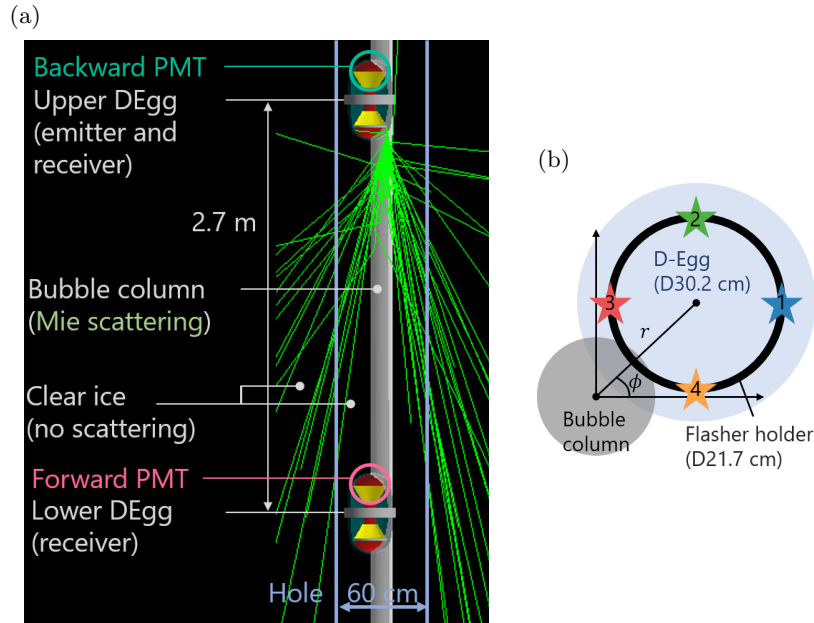


**Figure 5.5:** a) Illustration of the simulation: two D-Egg modules are located (partially) inside the bubble column. Photons from the LED originating from the upper D-Egg module are Mie scattered in the bubble column. b) Position parameters  $r$  and  $\phi$ . The stars represent the four downward-facing LEDs, LED1–4.  $\phi = 0$  when LED1 is the furthest from the center.

light source at a wavelength of 405 nm. The initial directions of photons  $(\theta, \phi)$  are sampled from two uniform distributions; uniform in  $\theta$  from  $0^\circ$  to  $30^\circ$  and in  $\phi$  from  $0^\circ$  to  $360^\circ$ . The photons are weighted in order to mimic the target angular profile afterward. The configuration in Figure 5.6 is used as the default profile in this study.

### 5.2.4.3 Detection efficiency

The photons emitted from the LED experience absorption in the gel, glass, and ice, as well as reflection and refraction at the boundary between different materials (see Section 4.2). Importantly, the photons also undergo scattering in the bubble column as modeled in Section 5.2.2. In the simulation, when the photons hit the photocathode of either the forward or backward PMT, their initial direction  $\theta$  and the hit positions on the photocathode  $\mathbf{r}$  are recorded. After the simulation, the hit photons are weighted to mimic the angular profile of the LED (see Section 5.2.4.2). The weight is

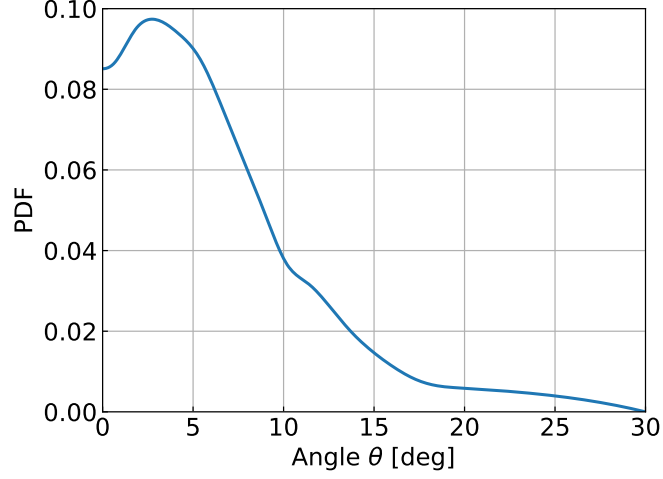


**Figure 5.6:** Angular profile of LED XRL-400-5O measured by Jack Nuckles [27]. Although the measurement was performed for both sides (angle  $0^\circ$  to  $30^\circ$  and  $0^\circ$  to  $-30^\circ$ ), their average is shown since the intensity is considered to be uniform over azimuth.

calculated using the photon's initial direction  $\theta$  ( $0^\circ \leq \theta \leq 30^\circ$ ):

$$w(\theta) = p_{\text{LED}}(\theta)/p_{\text{sim}}(\theta) , \quad (5.5)$$

where  $p_{\text{LED}}$  is a probability density function (PDF) of the angular profile of the XRL-400-5O, and  $p_{\text{sim}}$  is a PDF of  $\theta$  in the simulation, thus  $p_{\text{sim}}(\theta) = \frac{1}{30}[\text{deg}]^{-1}$ .

In addition, the hit photons are weighted to be converted into photoelectrons (PEs) by including the PMT response. The weight for a photon which arrives at the position on the PMT cathode  $\mathbf{r}$  is given as

$$w(\mathbf{r}) = \text{QE} \times \text{CE}(\mathbf{r}) . \quad (5.6)$$

The PMT SQ0262 is assumed in this study since it has a typical performance among the PMTs measured in the laboratory, which has 36.725% QE at a wavelength of 405 nm and CE averaged over azimuth shown in Figure 5.7. The NPE detected by the forward PMT and the backward PMT is then calculated by summing the weighted photons, to eventually extract the hole ice parameters.

#### 5.2.4.4 Results – Hole ice parameter dependence of NPE

From the simulation the expected NPE has been calculated over a large range of the effective scattering length in the bubble column  $\lambda_s$ , bubble

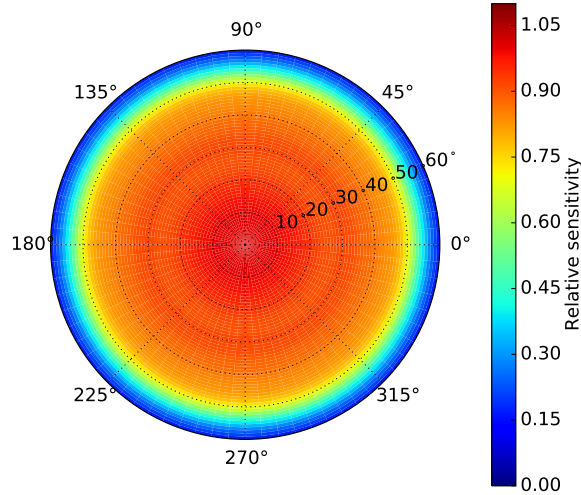
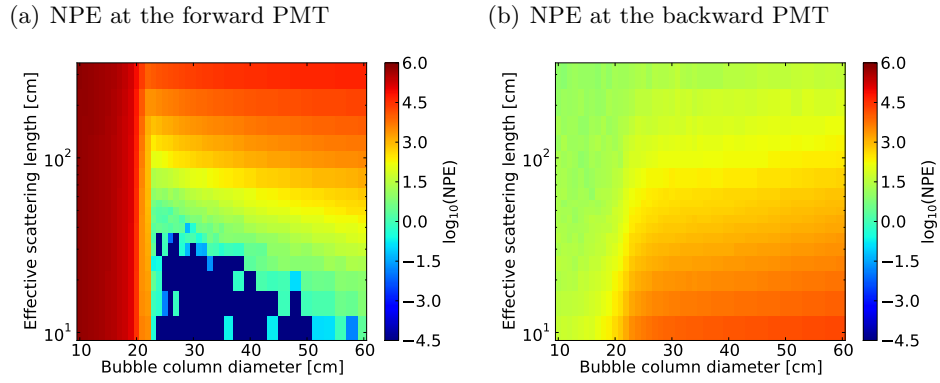


**Figure 5.7:** Measured detection uniformity of PMT SQ0262 averaged over azimuth, normalized to the center. In this study the relative sensitivity is assumed to be equal to the uniformity (see Section 3.2.3).

column diameter  $D$ , and the position of the D-Eggs  $r, \phi$ , for both the forward and backward PMTs  $n^F$  and  $n^B$ , respectively (see Figure 5.5(b)).

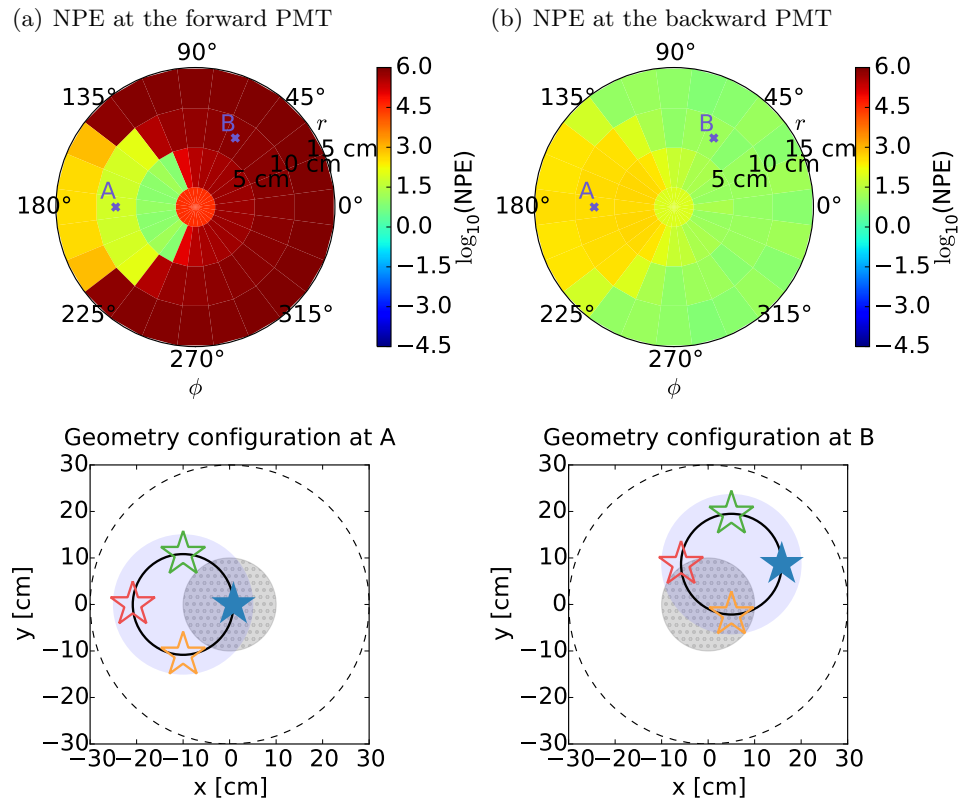
Figure 5.8 shows the NPE dependence on  $\lambda_e$  and  $D$ , where the D-Eggs are at the center of the bubble column ( $r = 0$ ). Figure 5.8(a) indicates that the bubble column diameter dependence of  $n^F$  changes after  $D$  exceeds approximately 20 cm. In cases when the bubble column is smaller than around 20 cm, the smaller bubble column detects more PEs, as the majority of photons hit the PMT directly, avoiding the bubble column entirely. However if  $D \gtrsim 20$  cm, the bubble column covers the LED, trapping the photons, resulting in increased detection for thick bubble columns. Figure 5.8(b) shows the backward PMT detects more PEs when the scattering length becomes shorter as well as when the bubble column becomes larger. This is independent of whether the LED is inside or outside the bubble column, because the backward PMT observes photons which have undergone scattering in the bubble column.

Figure 5.9 describes the NPE dependence on the position  $r$  and  $\phi$  where the bubble column is 20 cm in diameter and LED1, which is located in the direction of  $\phi = 0^\circ$  (see Figure 5.5(b)), flashes. In the case of the



**Figure 5.8:**  $\lambda_e$  and  $D$  dependence of NPE out of  $2 \times 10^7$  photons incidence when  $r = 0$ .

forward PMT, the NPE increases as the LED moves further from the bubble column, because of reduced photon scattering. Conversely, the backward PMT detects more PEs as the LED approaches the bubble column, because the bubble column acts as a light-guide to the PMT.



**Figure 5.9:** Top:  $r$  and  $\phi$  dependence of NPE out of  $2 \times 10^7$  photons incidence when  $\lambda_e = 30$  cm,  $D = 20$  cm and LED1, which is represented as the blue star, flashes. Bottom: geometry configuration of the bubble column and the D-Egg's four LEDs when the center of the D-Eggs is at A and B marked in the top figures.

### 5.3 Systematic uncertainties

The effect of the detector response, the position of the D-Eggs in the hole, the brightness of the LEDs, the angular profile of the LEDs, light obstruction from the main cable and the choice of  $\langle \cos \theta \rangle$  are considered in this study. The detector uncertainties are included in both the pseudo experiments and the test data, meaning they have been taken into account through the entire analysis. The uncertainty in the position of the D-Eggs in the hole is included by introducing the nuisance parameters  $r$  and  $\phi$  (see Section 5.2.4.1), considered in Section 5.5.3 and beyond. The impact of the other uncertainties are quantified independently using test data generated from each extreme scenario in Section 5.5.4.

#### 5.3.1 Detector response

PMT saturation can be dealt with by lowering the gain of the PMTs. Alternatively, the NPE for the target incident photons can be obtained by flashing the LED with dimmer brightness more times. These ways are left, but this study conservatively assumes that the PMTs do not readout more than 300 PEs, which is almost in the range where the PMT response is linear at the normal gain  $10^7$  (see Figure 3.9(c)).

A Gaussian distribution with a standard deviation of 20% is applied to the other overall detector uncertainties such as the detection uniformity and the charge resolution of the PMTs.

#### 5.3.2 Alignment of the D-Eggs

As shown in Section 5.2.4.4, the NPE largely depends on the position of the LEDs, relative to the hole central axis, although the exact position is not the parameter of interest in the hole ice calibration. Therefore the position parameters  $r, \phi$  are included as nuisance parameters in this study.

That said, the orientation of the D-Eggs can also cause a large modification to the NPE. This systematic uncertainty will be solved by the inclinometer mounted to the D-Egg module, providing extra information regarding the alignment of the D-Eggs. However this uncertainty is not considered in this study. This systematic uncertainty is considered as an addition to the situation.

### 5.3.3 Flasher LED profiles

**Brightness** Recent studies on the D-Egg’s flasher system indicate that the brightness is consistent with a standard deviation of 4% and a mean drift of less than 1% [28]. However, the mean brightness of each LED is difficult to be calibrated accurately and has a variation of approximately 30%. The effect of the variance in LED by LED brightness is included by generating test data from the LEDs with a brightness of 70% or 130% of the assumption with a nominal brightness of  $1 \times 10^7$  photons/flash.

**Angular profile** Each LED has a unique angular profile as seen in Figure 5.10. Although as many LEDs as possible will be measured, knowing

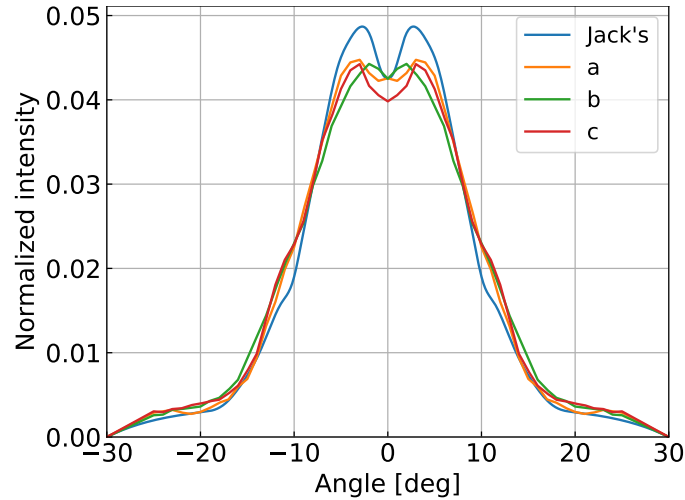


**Figure 5.10:** The default angular profile “Jack’s”, and the angular profile of other three LEDs, “a”, “b” and “c”, measured in Chiba. Although the measurement was performed for both sides (angle  $0^\circ$  to  $30^\circ$  and  $0^\circ$  to  $-30^\circ$ ), their average is shown since the intensity is considered to be uniform over azimuth.

the true angular profile of all of the LEDs is too time consuming.

In order to estimate the systematic error due to differences between the true angular profile and an assumed one, the three angular profiles “a”, “b”, “c” are tested assuming “Jack’s” is true.

### 5.3.4 Cable shadow

The D-Eggs will be deployed in the holes tied to a thick cable. If the cable is in the same direction  $\phi$  as one of the four LEDs, the LED may not be usable since light from the LED will be blocked by the cable. This effect is referred to as cable shadow. However, as mentioned in Section 3.1, the

D-Egg module also includes three cameras looking horizontally (Figure 5.11) for calibration purposes [29]. It is expected that the cameras will be able to determine the location of the cable. Thus, the cable shadow is included



**Figure 5.11:** Cameras in a D-Egg.

by creating test data sets where only three of the four LEDs are usable, assuming the LED blocked by the cable is known from analyzing data from the cameras.

### 5.3.5 $\langle \cos \theta \rangle$

As discussed in Section 5.2.2, the effective scattering length is a mix of the geometrical scattering length  $\lambda_s$  and the average cosine of the scattering angle  $\langle \cos \theta \rangle$ . In this study  $\langle \cos \theta \rangle = 0.95$  is used as default, however the true number is not known. The cases where the true  $\langle \cos \theta \rangle$  is different from the assumption are taken into account by generating test data with various combinations of  $\lambda_s$  and  $\langle \cos \theta \rangle$ , but resulting in the same  $\lambda_e$ .

## 5.4 Extraction of hole ice parameters

### 5.4.1 Analysis method

#### 5.4.1.1 Likelihood construction

From the simulation, the NPE detected for both the forward and backward PMTs has been calculated over a large range of  $\lambda_s$ ,  $D$ ,  $r$  and  $\phi$ .

A likelihood fit test was performed in order to understand how precisely the hole ice parameters can be estimated. To construct the PDF of  $R = n^F/n^B$ , the following assumptions are used:

- NPE follows a Poisson distribution with the mean NPE determined from simulations as a function of the LED intensity.
- The statistical uncertainty in the simulation is included by modifying the Poisson distribution using the weights  $w$  for each photon (see Eq. (5.5) and Eq. (5.6)). The probability of  $k$  photoelectrons being detected for a given set of parameters  $\Theta$  is written as:

$$P_{\text{eff}}(k|\Theta) = \left(\frac{\mu}{\sigma^2}\right)^{\frac{\mu^2}{\sigma^2}+1} \Gamma\left(k + \frac{\mu^2}{\sigma^2} + 1\right) \left[ k! \left(1 + \frac{\mu}{\sigma^2}\right)^{k + \frac{\mu^2}{\sigma^2} + 1} \Gamma\left(\frac{\mu^2}{\sigma^2} + 1\right) \right]^{-1} \quad (5.7)$$

where  $\mu = n^{\text{F(B)}} = \sum_{i=1}^{N_{\text{hit}}^{\text{F(B)}}} w_i^{\text{F(B)}}$  is the number of photoelectrons calculated from the simulation, and  $\sigma^2 = \sum_{i=1}^{N_{\text{hit}}^{\text{F(B)}}} w_i^{\text{F(B)2}}$ .  $\mu$  and  $\sigma^2$  depend on  $\Theta$  through  $w$ . Eq. (5.7) is adopted from [30].

- The detector response represented by the charge resolution is characterized by a Gaussian distribution with a standard deviation of 20%.

Figure 5.12 shows a NPE distribution at each step. The Poisson distribution is widened by Eq. (5.7) and the Gaussian distribution.

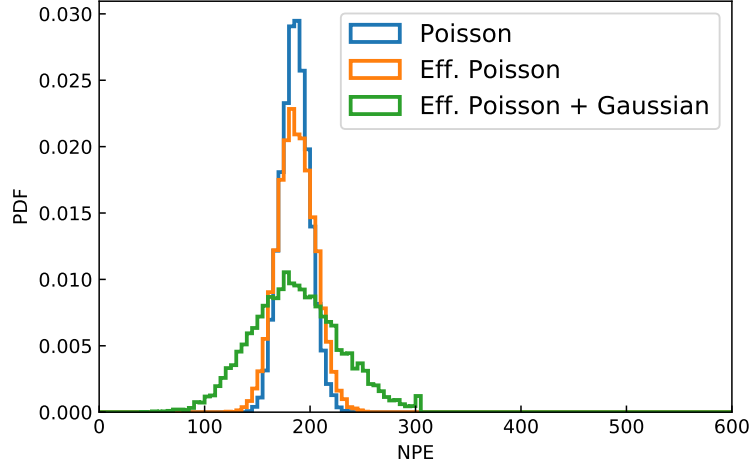


**Figure 5.12:** Example of a PDF of NPE. NPE sampled from a normal Poisson distribution is shown as the blue histogram. The orange histogram shows the NPE distribution sampled from a modified Poisson distribution (Eq. (5.7)), and the NPE is re-sampled from a Gaussian distribution with a standard deviation of 20% centered at the NPE, making the green histogram.

To perform a likelihood fit, the likelihood  $\mathcal{L}$  for test data  $\mathbf{x}$  and a given set of floating parameters  $\Theta$  is constructed as:

$$\mathcal{L}(\mathbf{x}|\Theta) = \prod_{l=1}^4 \prod_{i=1}^{N_{\text{evt}}} p_{\Theta}^l(x_i^l), \quad (5.8)$$

where  $l$  is the LED number,  $i$  is the event number, and  $N_{\text{evt}} (= 100)$  is the number of events.  $x_i^l = \log_{10} R_i^l$  from the test data.  $\Theta$  is a vector composed of the four hole ice parameters.  $p_{\Theta}^l$  is the PDF of  $\log_{10} R_{\Theta}^l$ .

#### 5.4.1.2 Test statistic

The log likelihood ratio is used as the test statistic:

$$\mathcal{TS}(\Theta) = \ln \frac{\mathcal{L}(\hat{\Theta})}{\mathcal{L}(\Theta)}, \quad (5.9)$$

where

$$\hat{\Theta} = \underset{\Theta}{\operatorname{argmax}} \mathcal{L}(\Theta). \quad (5.10)$$

When  $r, \phi$  of  $\Theta = (\lambda_e, D, r, \phi)$  are treated as nuisance parameters,

$$\mathcal{TS}(\lambda_e, D) = \ln \frac{\mathcal{L}(\hat{\Theta})}{\mathcal{L}(\lambda_e, D, \hat{r}, \hat{\phi})}, \quad (5.11)$$

where

$$(\hat{r}, \hat{\phi}) = \underset{(r, \phi)}{\operatorname{argmax}} \mathcal{L}(\lambda_e, D, r, \phi). \quad (5.12)$$

The test statistic distribution for each parameter  $\Theta$  is generated by performing a pseudo experiment  $10^4$  times (Figure 5.13).

The p-value for a test statistic  $\mathcal{TS}(\mathbf{x}|\Theta)$  calculated for observed data  $\mathbf{x}$  is calculated as:

$$p_{\text{value}}(\Theta) = \mathbb{P}(\mathcal{TS}(\Theta) > \mathcal{TS}(\mathbf{x}|\Theta)), \quad (5.13)$$

and  $p_{\text{value}} = 0.3173, 0.0455, 0.0027$  correspond to the confidence level (CL) of  $1\sigma, 2\sigma, 3\sigma$ , respectively.

In the case where  $r$  and  $\phi$  of  $\Theta = (\lambda_e, D, r, \phi)$  are treated as nuisance parameters, the test statistic distribution for a  $(\lambda_e, D)$  depends on the true value of  $(r, \phi)$ . At a  $(\lambda_e, D)$ , the p-value is calculated for every  $(r, \phi)$ , and the maximum is chosen as the p-value at the  $(\lambda_e, D)$  bin:

$$p_{\text{value}}(\lambda_e, D) = \max_{(r, \phi)} \mathbb{P}(\mathcal{TS}(\lambda_e, D, r, \phi) > \mathcal{TS}(\mathbf{x}|(\lambda_e, D))). \quad (5.14)$$

#### 5.4.1.3 Test data

Test data are generated based on the assumptions described in Section 5.4.1.1 (Figure 5.14).

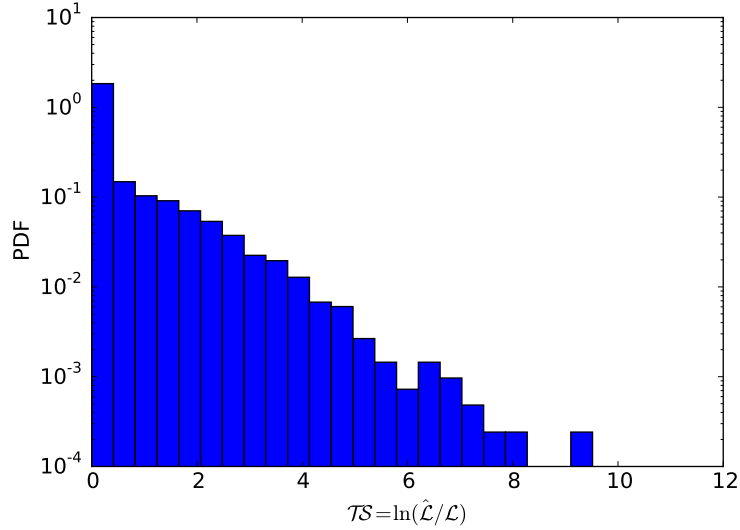


**Figure 5.13:** Example of the test statistic distribution, when  $\lambda_e = 30$  cm,  $D = 20$  cm,  $r = 10$  cm,  $\phi = 45^\circ$ , and  $r$  and  $\phi$  are treated as nuisance parameters. The distribution depends on the parameters  $\Theta$ , but most of the distributions have a sharp peak at zero, followed by a gradual decrease.

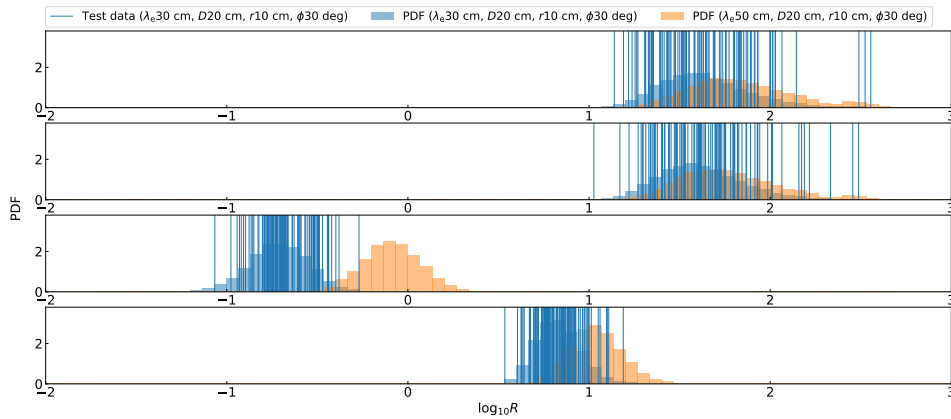


**Figure 5.14:** Example of the PDF of  $R$  for flashing LED1, 2, 3 and 4 from top to bottom when  $\lambda_e = 30$  cm,  $D = 20$  cm,  $r = 10$  cm,  $\phi = 30^\circ$  are shown with test data of 100 events for this MC truth shown in blue, and the PDF of  $R$  for another parameter ( $\lambda_e = 50$  cm,  $D = 20$  cm,  $r = 10$  cm,  $\phi = 30^\circ$ ) in orange.

## 5.5 Results

### 5.5.1 Case study – Three scenarios

In this section, the results of likelihood fit tests three true geometrical scenarios (Figure 5.15) are shown:

**Scenario  $\mathcal{A}$**  ( $\lambda_e = 30$  cm,  $D = 20$  cm,  $r = 0$ )

**Scenario  $\mathcal{B}$**  ( $\lambda_e = 30$  cm,  $D = 20$  cm,  $r = 10$  cm,  $\phi = 30^\circ$ )

**Scenario  $\mathcal{C}$**  ( $\lambda_e = 30$  cm,  $D = 50$  cm,  $r = 10$  cm,  $\phi = 30^\circ$ )

Comparison of Scenario  $\mathcal{A}$  with Scenario  $\mathcal{B}$  can reveal differences between cases where the position of D-Eggs is symmetric and asymmetric to the bubble column.  $D = 20$  cm was chosen because it is comparable to what has been observed by the Swedish camera. However, it is hard to imagine that D-Eggs will be placed just at the center of the bubble column, which is why Scenario  $\mathcal{C}$  was also chosen to be asymmetric. In Scenario  $\mathcal{C}$  a large bubble column was chosen because it is similar to the current hole ice model used in IceCube, which considers that the optical properties are uniform in the entire hole ice. In the current hole ice model  $\lambda_e = 50$  cm is used.  $\lambda_e$  in the bubble column should be shorter than in the outer region of the hole ice, thus  $\lambda_e = 30$  cm is commonly chosen in this study.

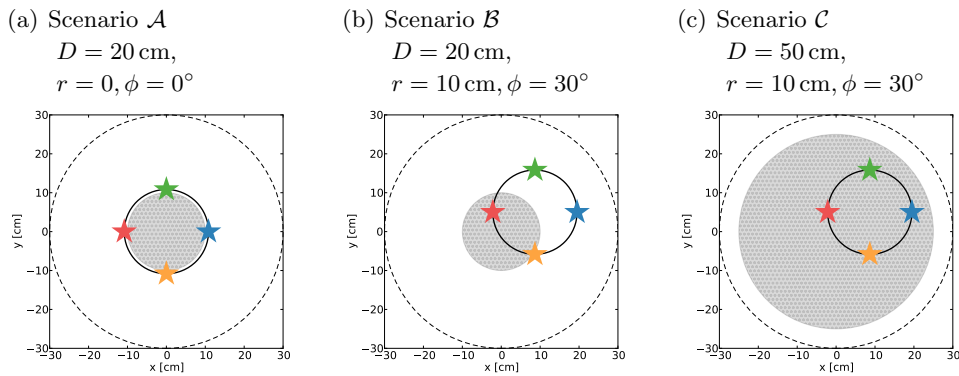


**Figure 5.15:** True scenarios tested. The gray circle represents the bubble column, and the dashed circle shows the size of the hole, where D-Eggs can locate inside. The four stars represent the LEDs on the flasher board shown as a black circle. Their colors correspond to Figure 5.5(b).

### 5.5.2 A case when the geometrical information is available

Firstly, a likelihood fit test was performed assuming the true values of  $r, \phi$  ( $r_{\text{true}}, \phi_{\text{true}}$ ) are known. This situation could be achieved by some independent measurement utilizing other calibration modules such as cameras

in the D-Eggs. For simplicity, no other systematic uncertainties except for the detector response was considered.

Figure 5.16 shows the p-value for each scenario. The true hole ice parameters, the effective scattering length and the bubble column diameter, are always covered by the  $1\sigma$  confidence region. In Scenario  $\mathcal{A}$ , the best fit is found in the same bin as the MC truth, however, the confidence region of the effective scattering length and the bubble column diameter distributes as a curved band over a large range of the parameters because the degeneracy of the two parameters cannot be solved due to the symmetry of the position of the D-Eggs to the bubble column. In Scenario  $\mathcal{B}$  and  $\mathcal{C}$ , the hole ice parameters are found to be within the same bin as the MC truth at  $3\sigma$  CL.

### 5.5.3 A case when no external information is available

Secondly, a likelihood fit test was performed for the case where the position of the D-Eggs in the hole  $(r, \phi)$  is not known. Other conditions are still the same as Section 5.5.2.

Figure 5.17 shows the p-value for each MC truth value. In all cases, the best fit values for  $\lambda_e$  and  $D$  are found in the  $1\sigma$  confidence region. The confidence region is larger than Figure 5.16 because of the indefiniteness of the nuisance parameters,  $(r, \phi)$ . If the situation will be similar to Scenario  $\mathcal{B}$  or Scenario  $\mathcal{C}$ , the effective scattering length and the bubble column diameter are determined within  $\pm 5$  cm and  $\pm 1$  cm, respectively, at  $3\sigma$  CL even if no external information of the position of the D-Eggs is available.

### 5.5.4 Final result: all systematic uncertainties included

In the case where  $r_{\text{true}}$  and  $\phi_{\text{true}}$  are unknown, likelihood fits were performed for test data generated from different assumptions than those assumed in the fits. Figure 5.18–5.21 show the expected largest impact from the systematic uncertainties in the brightness of the LEDs, the angular profile of the LEDs, the cable shadow and  $\langle \cos \theta \rangle$ , respectively. The sparse confidence regions in some of them are due to the coarse binning of the parameters as well as the impact from the multiple tested scenarios. For example, in Figure 5.20(b), the  $3\sigma$  confidence region is dominated by the case where the light from LED3 or LED4 is obstructed by the main cable. As these LEDs are inside or close to the bubble column in Scenario  $\mathcal{B}$ , the lack of information from either of them results in the degeneracy between  $\lambda_e, D$  and  $r, \phi$ . If  $r_{\text{true}}$  and  $\phi_{\text{true}}$  are given,  $\lambda_e$  and  $D$  can be determined within the MC truth bin.

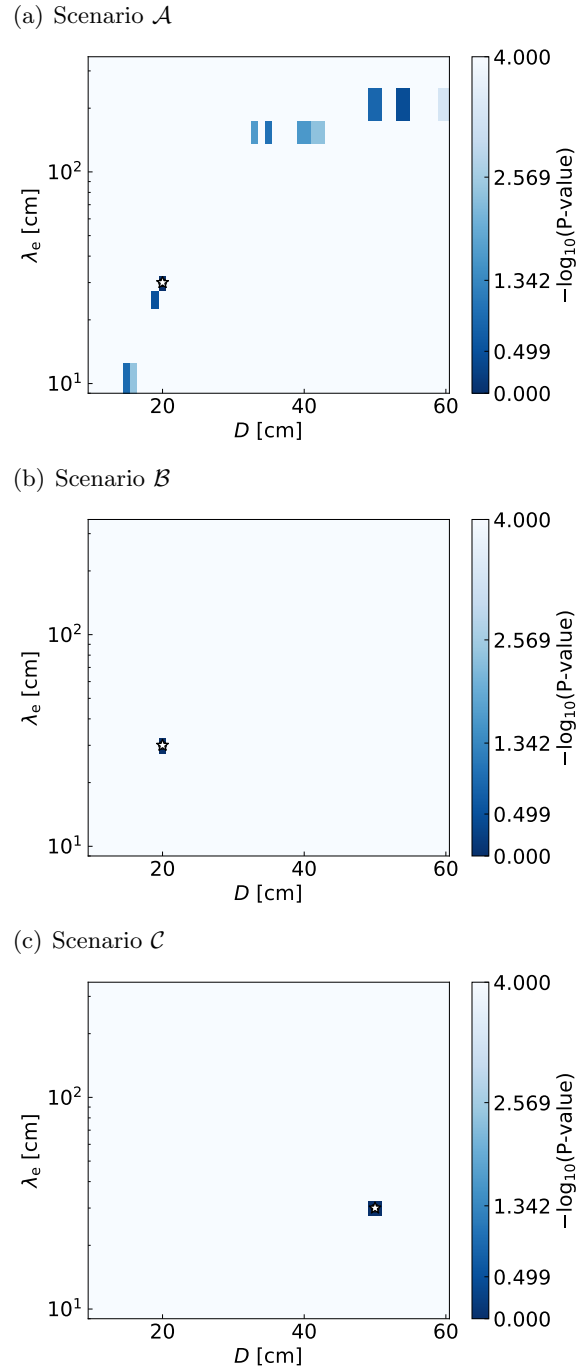


**Figure 5.16:** Results of likelihood fit tests where  $r_{\text{true}}, \phi_{\text{true}}$  are known. The shown  $-\log_{10} p_{\text{value}}$  values between 0.0 and 4.0 correspond to  $1\sigma, 2\sigma$  and  $3\sigma$  from bottom to top. P-value can be shown up to 0.0001 due to the number of pseudo experiments done for generating the test statistic distributions. The MC truth is marked with a white circle and the best fit bin with a white star.

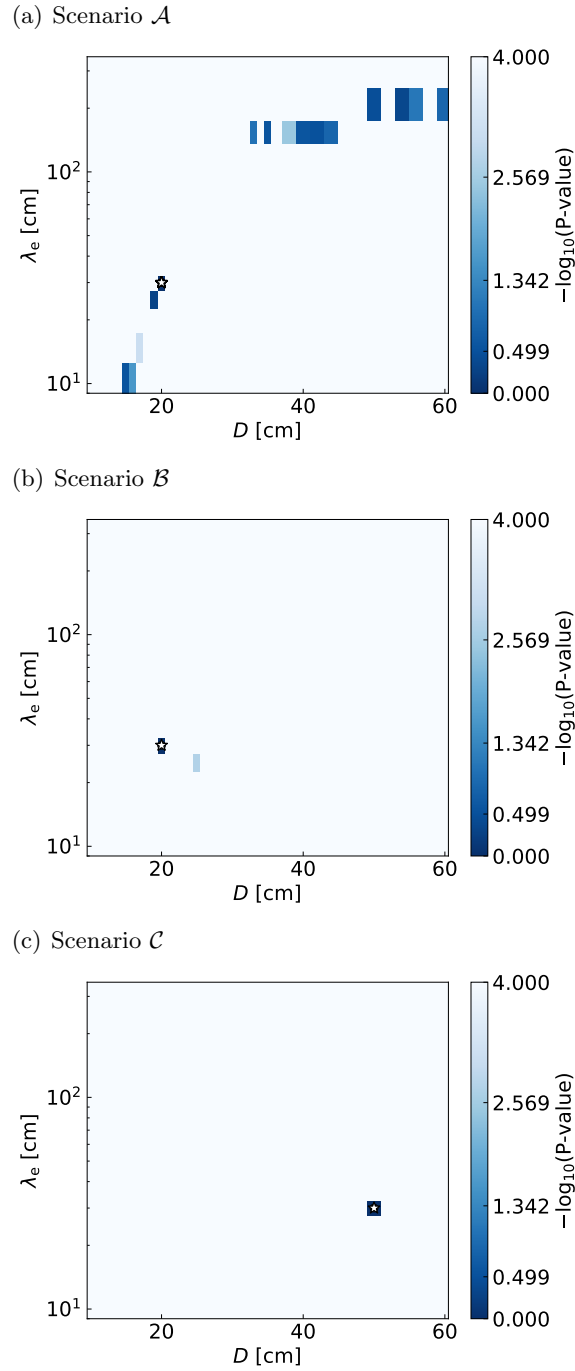


**Figure 5.17:** Results of likelihood fit tests where  $r_{\text{true}}, \phi_{\text{true}}$  are unknown. The shown  $-\log_{10} p_{\text{value}}$  values between 0.0 and 4.0 correspond to  $1\sigma, 2\sigma$  and  $3\sigma$  from bottom to top. P-value shown is limited to 0.0001 by the number of pseudo experiments,  $10^4$ , performed for generating the test statistic distributions. The MC truth is marked with a white circle and the best fit bin with a white star.

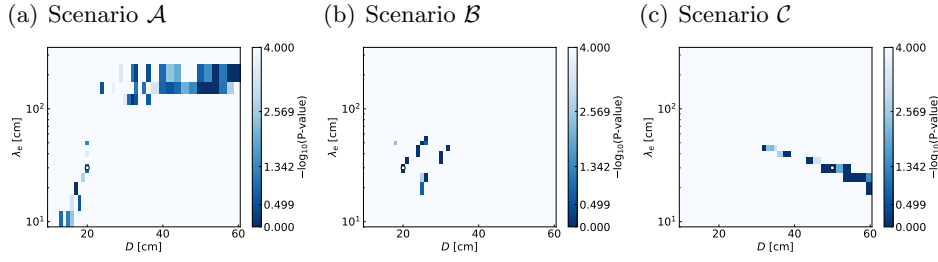


**Figure 5.18:** Largest p-values for test data from LEDs with +30% of  $-30\%$  of brightness. The MC truth is marked with a white circle.

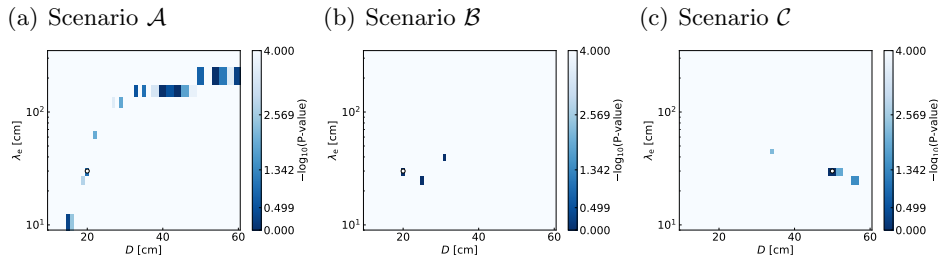


**Figure 5.19:** Largest p-values for test data from LEDs with a different angular profile. The MC truth is marked with a white circle.

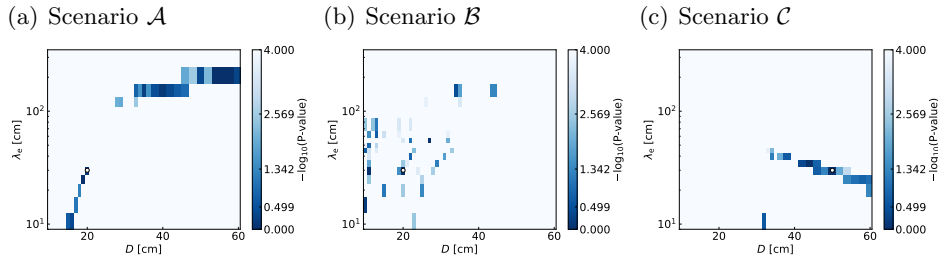


**Figure 5.20:** Largest p-values for test data from three LEDs out of four. The MC truth is marked with a white circle.

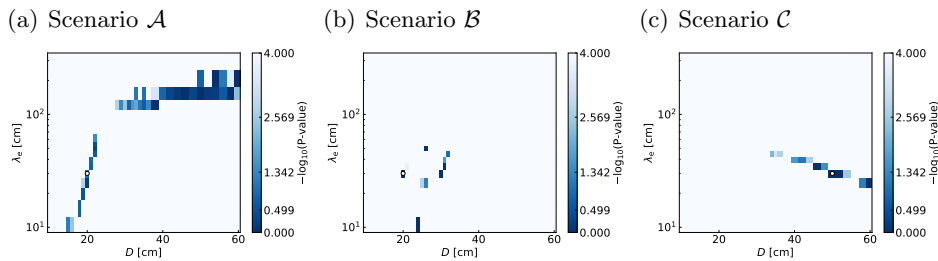


**Figure 5.21:** Largest p-values for test data from  $\langle \cos \theta \rangle$  from 0.7 to 0.9. The MC truth is marked with a white circle.

Figure 5.22 shows the final result including the all systematic uncertainties shown above. The confidence interval is calculated as a square root of sum of squares of the changes in the confidence intervals when each systematic uncertainty is fixed to the extreme value in turn with the others predictable from when no systematic uncertainty exists, as they are considered to be independent.

Figure 5.22(a) depicts Scenario  $\mathcal{A}$  where the D-Eggs are aligned at the center of the hole. In this case the small bubble column with a short scattering length and the large bubble column with a long scattering length are difficult to be distinguished due to the geometrical symmetry. However, the region where  $\lambda_e < 75$  cm and  $22$  cm  $< D < 60$  cm is excluded at  $3\sigma$  CL.

In Scenario  $\mathcal{B}$ , Figure 5.22(b) shows that the hole ice parameters are estimated to be within  $\lambda_e < 200$  cm and  $D < 46$  cm at  $3\sigma$  CL. The large confidence region is due to the systematic uncertainties in the position of the D-Eggs and the cable shadow.

In Scenario  $\mathcal{C}$ , Figure 5.22(c) describes the effective scattering length is determined to be  $\lambda_e < 50$  cm and the bubble column diameter  $31$  cm  $< D < 60$  cm at  $3\sigma$  CL. The cable shadowing the LED3 contributes to the confidence region around ( $\lambda_e = 10$  cm,  $D = 32$  cm). The confidence region primarily shows a band extending over a range of  $15$  cm  $< \lambda_e < 50$  cm and  $31$  cm  $< D < 60$  cm.

### 5.5.5 Discussion

The D-Egg's flashers have the potential to characterize the hole ice more precisely than in current IceCube, though the accuracy depends on the actual hole ice properties. If the D-Eggs are aligned at the center of the bubble column, the position of the D-Eggs is correctly determined to be at the center, but a small bubble column with a short scattering length and a large bubble column with a long scattering length are not distinguishable. However, the bubble column boundary is expected to be determined by the cameras installed in the D-Eggs. If it succeeds, the range of possible effective scattering lengths will be restricted, breaking this degeneracy.

Given the case where at least one of the four LEDs are inside the bubble column, the D-Egg's flashers can distinguish the small bubble column with a short scattering length and the large bubble column with a long scattering length. The more LEDs located inside the bubble column, the more precisely the effective scattering length can be estimated.

In any case, external information on the bubble column diameter can place another restriction on the range of possible effective scattering lengths.

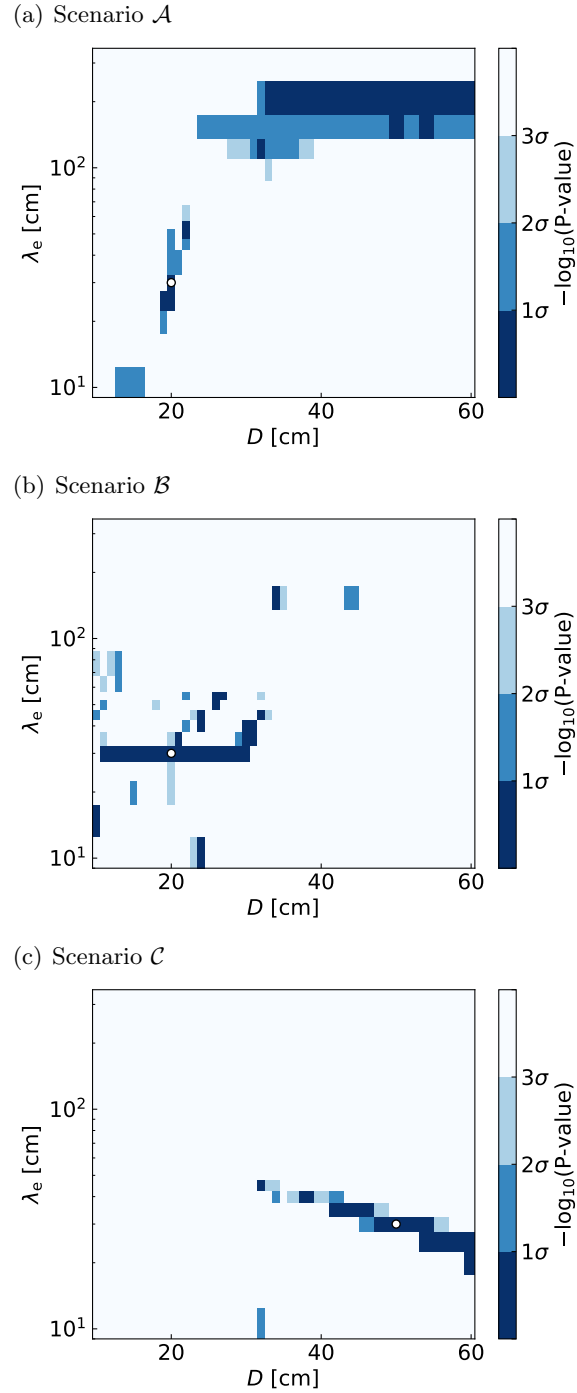


**Figure 5.22:** Results of likelihood fit tests where  $r_{\text{true}}, \phi_{\text{true}}$  are unknown and the systematic uncertainties are included. The MC truth is marked with a white circle.

For example, in Scenario  $\mathcal{C}$ , where the scattering length is only limited to a range shorter than 50 cm without any information on the bubble column diameter, the effective scattering length is limited to 20–40 cm if the cameras can determine the bubble column diameter within  $\pm 10\%$ .

Determining the hole ice parameters will be difficult if the bubble column is small and three or four LEDs are located outside the bubble column. In this case, other external light sources are necessary, such as mDOM’s flasher LEDs and the POCAM [18] [31].

Furthermore, the POCAM has LEDs with different wavelengths from 370 to 500 nm, which are useful for investigating the wavelength dependence of the Mie scattering in the bubble column. By performing the measurement with D-Egg’s flasher LEDs at all depths, the depth dependence of the optical properties of the hole ice will be able to be determined. Both wavelength and depth dependence of the optical properties of the hole ice will further improve neutrino reconstruction.

## 5.6 Conclusion

The D-Egg’s flashers have the potential to characterize the hole ice more precisely than in current IceCube, though the accuracy depends on the actual hole ice properties. If some of the LEDs are inside the bubble column, the D-Egg’s flashers can distinguish the small bubble column with a short scattering length and the large bubble column with a long scattering length. Precision can be further increased if more of the flasher LEDs are located inside the bubble column.

## Chapter 6

# Conclusion

The D-Egg will make use of the four downward-facing flasher LEDs to calibrate current IceCube models based on hole ice data collected in the IceCube Upgrade. In this analysis the hole ice was parameterized by the effective scattering length  $\lambda_e$  and the bubble column diameter  $D$ . The precise photon simulation and a maximum likelihood fit for three scenarios were performed to estimate how precisely the D-Egg's hole ice calibration system would determine the hole ice parameters.

The D-Egg's flashers have the potential to determine the hole ice parameters, but the accuracy depends on the actual hole ice properties. In Scenario  $\mathcal{A}$ , where the D-Eggs are at the center of the hole, the small bubble column with a short scattering length and the large bubble column with a long scattering length are difficult to distinguish due to the geometrical symmetry. However, the region where  $\lambda_e < 75$  cm and  $22$  cm  $< D < 60$  cm is excluded at  $3\sigma$  CL. In other cases, the D-Egg's flashers can estimate the hole ice parameters, within  $\lambda_e < 200$  cm and  $D < 46$  cm in Scenario  $\mathcal{B}$ , and  $\lambda_e < 50$  cm and  $31$  cm  $< D < 60$  cm in Scenario  $\mathcal{C}$  at  $3\sigma$  CL.

# Bibliography

- [1] Ulrich F Katz and Ch Spiering. High-energy neutrino astrophysics: Status and perspectives. *Progress in Particle and Nuclear Physics*, 67(3):651–704, 2012.
- [2] Mark Gerald Aartsen, R Abbasi, Yasser Abdou, M Ackermann, J Adams, JA Aguilar, M Ahlers, D Altmann, J Auffenberg, X Bai, et al. First observation of PeV-energy neutrinos with IceCube. *Physical review letters*, 111(2):021103, 2013.
- [3] IceCube Collaboration et al. Neutrino emission from the direction of the blazar TXS 0506+ 056 prior to the IceCube-170922A alert. *Science*, 361(6398):147–151, 2018.
- [4] MG Aartsen, R Abbasi, Yasser Abdou, M Ackermann, J Adams, JA Aguilar, M Ahlers, D Altmann, J Auffenberg, X Bai, et al. Measurement of South Pole ice transparency with the IceCube LED calibration system. *Nuclear Instruments and Methods in Physics Research Section A: Accelerators, Spectrometers, Detectors and Associated Equipment*, 711:73–89, 2013.
- [5] MG Aartsen, M Ackermann, J Adams, JA Aguilar, M Ahlers, M Ahrens, D Altmann, K Andeen, T Anderson, I Anseau, et al. Measurement of atmospheric tau neutrino appearance with IceCube DeepCore. *Physical Review D*, 99(3):032007, 2019.
- [6] Thomas K Gaisser, Ralph Engel, and Elisa Resconi. *Cosmic rays and particle physics*. Cambridge University Press, 2016.
- [7] MG Aartsen, M Ackermann, J Adams, JA Aguilar, M Ahlers, M Ahrens, D Altmann, K Andeen, T Anderson, I Anseau, et al. The IceCube Neutrino Observatory: instrumentation and online systems. *Journal of Instrumentation*, 12(03):P03012, 2017.

- [8] Francis Halzen and Spencer R Klein. Invited review article: IceCube: an instrument for neutrino astronomy. *Review of Scientific Instruments*, 81(8):081101, 2010.
- [9] IceCube Collaboration et al. Evidence for high-energy extraterrestrial neutrinos at the IceCube detector. *Science*, 342(6161):1242856, 2013.
- [10] Rasha Abbasi, Yasser Abdou, T Abu-Zayyad, M Ackermann, J Adams, JA Aguilar, M Ahlers, MM Allen, D Altmann, K Andeen, et al. The design and performance of IceCube DeepCore. *Astroparticle physics*, 35(10):615–624, 2012.
- [11] MG Aartsen, R Abbasi, Yasser Abdou, M Ackermann, J Adams, JA Aguilar, M Ahlers, D Altmann, J Auffenberg, X Bai, et al. Measurement of South Pole ice transparency with the IceCube LED calibration system. *Nuclear Instruments and Methods in Physics Research Section A: Accelerators, Spectrometers, Detectors and Associated Equipment*, 711:73–89, 2013.
- [12] T Benson, J Cherwinka, M Duvernois, A Elcheikh, F Feyzi, L Greenler, J Haugen, A Karle, M Mulligan, and R Paulos. IceCube enhanced hot water drill functional description. *Annals of Glaciology*, 55(68):105–114, 2014.
- [13] P Buford Price and K Woschnagg. Role of group and phase velocity in high-energy neutrino observatories. *Astroparticle Physics*, 15(1):97–100, 2001.
- [14] F Bos, F Tenholt, J Becker Tjus, and S Westerhoff. Observation of the cosmic-ray shadow of the moon and sun with icecube. *ASTRA Proceedings*, 2:5, 2015.
- [15] Martin Rongen. Measuring the optical properties of IceCube drill holes. In *EPJ Web of Conferences*, volume 116, page 06011. EDP Sciences, 2016.
- [16] Aya Ishihara. The IceCube Upgrade–Design and Science Goals. *arXiv preprint arXiv:1908.09441*, 2019.
- [17] MG Aartsen, M Ackermann, J Adams, JA Aguilar, M Ahlers, M Ahrens, D Altmann, T Anderson, G Anton, C Argüelles, et al. IceCube-Gen2: a vision for the future of neutrino astronomy in Antarctica. *arXiv preprint arXiv:1412.5106*, 2014.

- [18] MG Aartsen, M Ackermann, J Adams, JA Aguilar, M Ahlers, M Ahrens, I Al Samarai, D Altmann, K Andeen, T Anderson, et al. The IceCube Neutrino Observatory-Contributions to ICRC 2017 Part VI: IceCube-Gen2, the Next Generation Neutrino Observatory. *arXiv preprint arXiv:1710.01207*, 2017.
- [19] Satoshi Shimizu, Achim Stoessl, Shigeru Yoshida, and Aya Ishihara. Overview and performance of the D-Egg optical sensor for IceCube-Gen2. *PoS*, page 1051, 2017.
- [20] <https://www.hitachi-metals.co.jp/products/elec/tel/pdf/h1-fm9-h.pdf>.
- [21] Hamamatsu Photonics. [https://www.hamamatsu.com/resources/pdf/etd/PMT\\_handbook\\_v3aE.pdf](https://www.hamamatsu.com/resources/pdf/etd/PMT_handbook_v3aE.pdf).
- [22] [http://www.roithner-laser.com/datasheets/led\\_div/xrl-400-5o.pdf](http://www.roithner-laser.com/datasheets/led_div/xrl-400-5o.pdf).
- [23] Kotoyo Hoshina. DOMINANT. <http://www.ppl.phys.chiba-u.jp/research/IceCube/DetectorSim/DOMINANT/>.
- [24] J Allison, Katsuya Amako, J Apostolakis, Pedro Arce, M Asai, T Aso, E Bagli, A Bagulya, S Banerjee, G Barrand, et al. Recent developments in Geant4. *Nuclear Instruments and Methods in Physics Research Section A: Accelerators, Spectrometers, Detectors and Associated Equipment*, 835:186–225, 2016.
- [25] Louis G Henyey and Jesse L Greenstein. Diffuse radiation in the galaxy. *The Astrophysical Journal*, 93:70–83, 1941.
- [26] Markus Ackermann, J Ahrens, X Bai, M Bartelt, SW Barwick, RC Bay, T Becka, JK Becker, K-H Becker, P Berghaus, et al. Optical properties of deep glacial ice at the South Pole. *Journal of Geophysical Research: Atmospheres*, 111(D13), 2006.
- [27] Jack Nuckles. Private Communication, 2019.
- [28] Jack Nuckles. Private Communication, 2020.
- [29] Woosik Kang, Christoph Tönnis, and Carsten Rott. The camera system for the IceCube Upgrade. *arXiv preprint arXiv:1908.07734*, 2019.
- [30] Carlos A Argüelles, Austin Schneider, and Tianlu Yuan. A binned likelihood for stochastic models. *Journal of High Energy Physics*, 2019(6):30, 2019.

- [31] Martin Jurkovič, K Abraham, K Holzappel, K Krings, E Resconi, and J Veenkamp. A precision optical calibration module (POCAM) for IceCube-Gen2. In *EPJ Web of Conferences*, volume 116, page 06001. EDP Sciences, 2016.